# SIMULATED THERMAL PROTECTION TILE ROUGHNESS EFFECTS ON WINDWARD SURFACE HEAT TRANSFER ON THE ROCKWELL INTERNATIONAL SPACE SHUTTLE ORBITER

VON KÁRMÁN GAS DYNAMICS FACILITY
ARNOLD ENGINEERING DEVELOPMENT CENTER
AIR FORCE SYSTEMS COMMAND
ARNOLD AIR FORCE STATION, TENNESSEE 37389

January 1977

Final Report for Period November 14 — December 10, 1975

Prepared for

NATIONAL AERONAUTICS AND SPACE ADMINISTRATION (JSC)
HOUSTON, TEXAS 77058

This report has been reviewed by the Information Office (OI) and is releasable to the National Technical Information Service (NTIS). At NTIS, it will be available to the general public, including foreign nations.

## APPROVAL STATEMENT

This technical report has been reviewed and is approved for publication.

FOR THE COMMANDER

CHAUNCEY D. SMITH, JR.
Lt Colonel, USAF
Chief Air Force Test Director, VKF
Directorate of Test

ALAN L. DEVEREAUX
Colonel, USAF
Director of Test

# UNCLASSIFIED

| REPORT DOCUMENTATION PAGE | | READ INSTRUCTIONS BEFORE COMPLETING FORM |
|---|---|---|
| 1 REPORT NUMBER<br>AEDC-TR-76-98 | 2 GOVT ACCESSION NO. | 3 RECIPIENT'S CATALOG NUMBER |
| 4 TITLE (and Subtitle)<br>SIMULATED THERMAL PROTECTION TILE ROUGH-<br>NESS EFFECTS ON WINDWARD SURFACE HEAT<br>TRANSFER ON THE ROCKWELL INTERNATIONAL<br>SPACE SHUTTLE ORBITER | | 5 TYPE OF REPORT & PERIOD COVERED<br>Final Report, November<br>14-December 10, 1975 |
| | | 6 PERFORMING ORG REPORT NUMBER |
| 7 AUTHOR(s)<br>F. K. Hube, ARO, Inc. | | 8 CONTRACT OR GRANT NUMBER(s) |
| 9 PERFORMING ORGANIZATION NAME AND ADDRESS<br>Arnold Engineering Development Center (XO)<br>Air Force Systems Command<br>Arnold Air Force Station, Tennessee 37389 | | 10 PROGRAM ELEMENT, PROJECT, TASK AREA & WORK UNIT NUMBERS<br>Program Element 921E |
| 11 CONTROLLING OFFICE NAME AND ADDRESS<br>National Aeronautics and Space<br>Administration (JSC),<br>Houston, Texas 77058 | | 12 REPORT DATE<br>January 1977 |
| | | 13 NUMBER OF PAGES<br>61 |
| 14 MONITORING AGENCY NAME & ADDRESS(If different from Controlling Office) | | 15 SECURITY CLASS. (of this report)<br>UNCLASSIFIED |
| | | 15a DECLASSIFICATION DOWNGRADING SCHEDULE    N/A |

16 DISTRIBUTION STATEMENT (of this Report)

Approved for public release; distribution unlimited.

17 DISTRIBUTION STATEMENT (of the abstract entered in Block 20, if different from Report)

18 SUPPLEMENTARY NOTES

Available in DDC

19 KEY WORDS (Continue on reverse side if necessary and identify by block number)

aerodynamic heating
heat transfer
reentry vehicles
photographic techniques

spacecraft
orbit shuttle
materials
protection
thermal insulation

20 ABSTRACT (Continue on reverse side if necessary and identify by block number)
   Heat-transfer tests on the forward half of the 0.04-scale
models of the Rockwell International Space Shuttle Orbiter Con-
figuration 140C were conducted at Mach number 8.  Infrared
scanning was used to determine the influence of simulated thermal
protection tile roughness on windward surface heat-transfer level
and distribution.  Tile roughness was in the form of tile surface
mismatch and gaps between tiles.  Tile height (measured from the

DD FORM 1 JAN 73 1473    EDITION OF 1 NOV 55 IS OBSOLETE

# UNCLASSIFIED

20. ABSTRACT (Continued)

smooth body wall) ranged from -0.020 in. (cavity) to 0.025 in. (protuberance), and gap width ranged from 0 to 0.020 in. Data were obtained at angles of attack of 30 and 40 deg at zero side-slip at free-stream Reynolds numbers from $2.2 \times 10^6$ to $15.1 \times 10^6$ based on the total Orbiter scaled length. The infrared system is described, and data are presented which illustrate the influence of the major test parameters.

AFSC
Arnold AFS Tenn

# PREFACE

# CONTENTS

Page

3

# 1.0 INTRODUCTION

Tests have been performed on 4-percent scale models simulating the forward 50 percent of the Space Shuttle Orbiter to determine the influence of thermal protection tile roughness on windward surface heat-transfer distributions. Tile roughness was produced by tile surface joint mismatch and by gaps between the tiles. Combinations of gap width and tile height were tested, and the influence of tile axial location was investigated.

Earlier investigations of roughness influences on orbiter windward surface heating utilized the phase-change paint technique to measure wall temperature (Ref. 1). During these tests, it was found that great care had to be used to obtain a consistent, smooth painted surface which is required in transition studies. When planning the present test, it was decided that an alternate technique using an infrared (IR) scanning camera, which has no requirement for model coatings, would be considered. After an initial test run proved satisfactory, the IR technique was used for the entire test. This technique not only eliminated the need for painting but also provided on-line real-time color and gray-scale video screen display of the model temperature distributions as they developed. In addition, model centerline heat-transfer distributions were obtained from computer reduction of the data without the manual reduction required for phase-change paint data.

All data were obtained at Mach number 8 at angles of attack of 30 and 40 deg and free-stream Reynolds numbers ranging from $2.2 \times 10^6$ to $15.1 \times 10^6$ based on the scaled full orbiter length. Three axial tile locations were tested with tile heights ranging from -0.020 in. (cavity) to 0.025 in. (protuberance) and gap sizes from 0 to 0.020 in. Tests were conducted in the 50-in. Hypersonic Tunnel B of the von Kármán Gas Dynamics Facility (VKF). The infrared data system will be described, and selected data will be presented to illustrate the influence of the primary test parameters.

# 2.0 APPARATUS

## 2.1 WIND TUNNEL

Tunnel B is a closed-circuit hypersonic wind tunnel with a 50-in.-diam test section. Two axisymmetric contoured nozzles are available

7

to provide Mach numbers of 6 and 8, and the tunnel may be operated continuously over a range of pressure levels from 20 to 300 psia at $M_\infty$ = 6 and 50 to 900 psia at $M_\infty$ = 8, with air supplied by the VKF main compressor plant. Stagnation temperatures sufficient to avoid air liquefaction in the test section (up to 1,350°R) are obtained through the use of a natural-gas-fired combustion heater. The entire tunnel (throat, nozzle, test section, and diffuser) is cooled by integral, external water jackets. The tunnel is equipped with a model injection system, which allows removal of the model from the test section while the tunnel remains in operation. A description of the tunnel may be found in Ref. 2.

## 2.2 MODELS

The models were 0.040-scale models of the forward half of the Space Shuttle Orbiter 140C. Figure 1 shows a photograph of the basic model which was cast from Lockheed Proprietary Material "LH." Corresponding major model dimensions are presented in Fig. 2. A view of the lower surface in Fig. 3 shows a nickel-plated copper nose and stainless steel tile section installed.

The photograph in Fig. 4 shows the tile installation in detail. Stationary tiles were nominally 0.250-in. squares. Adjustable tiles installed for a 0.010-in. gap were 0.250-in. squares, while tiles used to achieve a 0.020-in. gap were 0.245-in. squares. It should be noted that gap changes were made only around the periphery of the adjustable tiles. All other gaps were fixed at 0.010 in. Figure 5 shows the tile vertical adjustment detail.

Three configurations with different axial locations of the simulated thermal protection tiles were tested. The sketch in Fig. 6 shows the axial location and angular orientation of the clusters of tiles. Configuration identifications are as follows:

| Configuration No. | Tile Location, $x/\ell$ |
|:---:|:---:|
| 6 | 0.050 |
| 7 | 0.111 |
| 8 | 0.175 |

where the reference length ($\ell$) is 4.311 ft (based on a full-scale length of 107.775 ft). Data in Ref. 3 indicated that streamwise oriented grooves

can trip the boundary layer. Consequently, the tiles are oriented to keep the grooves between the tiles at an angle to the flow direction. Tiles moved vertically during this test are indicated in Fig. 6. Note that this tile arrangement is not symmetrical about the model centerline.

Reference lines were painted on the model with an aluminum pigmented silicon paint, as can be seen in Figs. 3 and 4. The paint bands were approximately 0.200 in. wide and had an emissivity lower than the model material. Consequently, the lines appeared as cool bands on the infrared monitoring video screens and as points of apparent lower heating on the reduced digital data. After a few reference runs, a strip about 1 in. wide was cleaned along the model centerline to permit interference-free digital data to be obtained.

Chromel®-constantan thermocouples were installed in the copper nose section to monitor the forebody temperature ahead of the tiles during the test runs. Thermocouple locations are shown below:

| Thermocouple | $x/\ell$ Location | | |
|:---:|:---:|:---:|:---:|
| Number | No. 6 | No. 7 | No. 8 |
| 1 | 0.005 | 0.005 | 0.005 |
| 2 | 0.010 | 0.010 | 0.010 |
| 3 | 0.020 | 0.020 | 0.020 |
| 4 | 0.030 | 0.030 | 0.030 |
| 5 | --- | 0.050 | 0.050 |
| 6 | --- | 0.080 | 0.080 |
| 7 | --- | --- | 0.110 |
| 8 | --- | --- | 0.140 |

The copper nose reduced the wall temperature change ahead of the trip and minimized the boundary layer thickness growth during a run.

## 2.3 INFRARED SCANNING SYSTEM

### 2.3.1 Camera

Details of the infrared camera used in the VKF are illustrated in Fig. 7. Note that this is a scanning optical-mechanical camera which does not use film of any kind. The camera illustrated is manufactured in Sweden by AGA and is designated the Thermovision 680. Scan rate

is 16 frames/sec, and the detector is sensitive to radiation in the bandwidth from 2 to 5 $\mu$. The schematic in Fig. 8 shows the liquid-nitrogen-cooled (indium-antimonide) detector and the rotating prisms which control the position of the instantaneous field of view. A complete frame (one full scan) consists of 70 horizontal lines composed of 100 points each. Consequently, the field-of-view is mapped with 7,000 points.

Lenses for the Thermovision camera are made from germanium. This test was performed with a lens which had a viewing angle of 25 deg. The instantaneous field-of-view varies with the distance of the model from the camera.

Camera calibrations were performed with a commercially available reference blackbody. Calibrations have consistently been within ±1 percent of the camera manufacturer's standard calibration, and repeatability of calibrations has also been within ±1 percent. Temperature from ambient to 2,000°R can be measured. However, combinations of aperture size ("f" stop) and system sensitivity can be used to set appropriate full-scale values for maximum resolution. Check calibrations during the test did not show any significant variations.

## 2.3.2 Test Installation

Figure 9 illustrates the infrared camera installation in Tunnel B. The mirror arrangement is used instead of installing the camera vertically because of the liquid-nitrogen-filled Dewar which is filled from the top of the camera housing. An Irtran® window is used in the viewing path because the conventional materials used in wind tunnel windows are generally opaque to radiation in the 2- to 5-$\mu$ bandwidth. The Irtran window and mirror combination has a total transmittance of approximately 0.88. After the camera, window, and mirror are installed, a reference blackbody is installed in the tunnel test section to check the camera calibration.

## 2.3.3 Data System

A schematic of the data acquisition system used in this test is shown in Fig. 10. The camera output is recorded on analog tape and simultaneously transmitted to a CDC 1640B computer for on-line reduction. Real-time video display is available in both color and black and white. The color display presents the test model temperature distribution in ten colors. Photographs of the color screen display were obtained during each run. Between test runs, the analog

tape was replayed for additional visual examination and photography. Additional information about the system is available in Ref. 4.

## 2.4 INSTRUMENTATION AND PRECISION

Tunnel B stilling chamber pressure is measured with a 100- or 1,000-psid transducer referenced to a near vacuum. Based on periodic comparisons with secondary standards, the uncertainty (a bandwidth which includes 95 percent of residuals) of the transducers is estimated to be within $\pm 0.1$ percent of reading or $\pm 0.06$ psi, whichever is greater, for the 100-psid range and $\pm 0.1$ percent of reading or $\pm 0.5$ psi, whichever is greater, for the 1,000-psid range. Stilling chamber temperature measurements were made with Chromel®-Alumel® thermocouples which have an uncertainty of $\pm(1.5°F + 0.375$ percent of reading) based on repeat calibrations.

## 3.0 PROCEDURES

## 3.1 TEST CONDITIONS

Tests were conducted at the following free-stream conditions:

| $M_\infty$ | $P_O$, psia | $T_O$, °R | $Re_\ell \times 10^{-6}$ |
|---|---|---|---|
| 7.90 | 105 | 1,260 | 2.2 |
| 7.93 | 155 | 1,270 | 3.2 |
| 7.94 | 184 | 1,272 | 3.4 |
| 7.94 | 210 | 1,275 | 4.3 |
| 7.95 | 265 | 1,280 | 5.4 |
| 7.96 | 320 | 1,290 | 6.5 |
| 7.97 | 375 | 1,295 | 7.5 |
| 7.98 | 425 | 1,300 | 8.6 |
| 7.98 | 490 | 1,310 | 9.7 |
| 7.99 | 555 | 1,320 | 10.8 |
| 7.99 | 610 | 1,325 | 11.9 |
| 7.99 | 670 | 1,330 | 12.9 |
| 8.00 | 735 | 1,330 | 14.0 |
| 8.00 | 800 | 1,335 | 15.1 |

A complete test summary is presented in Table 1. A shadowgraph photograph was obtained during every run.

## 3.2 TEST PROCEDURE

Prior to each run, the model was cooled to a uniform initial model temperature of approximately 530°R. Effective cooling was accomplished by flowing cool water over the model surface. Model initial surface temperature was obtained with a thermocouple held in contact with the surface.

The cooled model was then injected into the tunnel flow at the desired angle of attack. Note that the model was mounted inverted to orient the windward surface toward the overhead camera. Data were recorded on analog tape continuously from the time the model was injected into the free stream until the color pattern on the video screen was fully developed. As the color pattern approached full development, a line of 70 points along the model centerline was digitized and transmitted to the CDC 1604. This procedure ensured that a sufficient temperature rise had occurred to provide good data precision while the visual monitoring showed that the camera output had not reached full scale. Run times generally ranged from 10 to 30 sec.

Color photographs of the color monitor screen were taken periodically during each run. When photographs were taken, a signal was recorded on the data record to obtain the time at which the photograph was taken.

## 3.3 DATA REDUCTION

Digitized model centerline data were reduced assuming the model to be a semi-infinite solid. After the camera output had been reduced to model wall temperature by using the blackbody calibration, the heat-transfer coefficient was obtained from the following expression:

$$h(T_o) = \beta(\rho C_p k)^{0.5}(t)^{-0.5} \tag{1}$$

where the value of $\beta$ is obtained by evaluating the following:

$$\frac{T_w - T_i}{T_o - T_i} = 1 - e^{\beta^2} \operatorname{erfc} \beta \tag{2}$$

The total elapsed model exposure time (t) was measured from the time the model entered the tunnel flow. Model material properties $((\rho C_p k)^{0.5})$ were obtained from a curve fit of values supplied by Rockwell

International. Figure 11 illustrates the variation in the model properties with temperature. The Fay-Riddell stagnation point heat-transfer coefficient (Ref. 5) ($h_{ref}$) based on a 0.04-ft-radius sphere, was used to normalize the computed aerodynamic heat-transfer coefficients.

The emissivity of Material "LH" was determined at AEDC and was found to be very nearly constant over the wavelength range of interest. Data reduction was performed with an emissivity value of 0.96.

During earlier paint tests using duplicate models without tiles, the model support sting was instrumented with strain gages to determine sting deflection. The results of the earlier work were curve fitted and entered in the present data reduction as an angle-of-attack correction.

Photographs of the color monitor screen are generally intended for qualitative analysis of temperature distributions. However, reduction of the photographic data along the color interfaces is very practical provided temperature, run time, and material properties are known.

## 4.0 PRECISION OF MEASUREMENTS

### 4.1 TEST CONDITIONS

Uncertainties of the basic tunnel flow parameters ($P_O$, $T_O$, and $M_\infty$) were estimated from repeat calibrations of the instruments and from repeatability and uniformity of the test section flow during tunnel calibrations. The individual contributions of these uncertainties were used to compute the uncertainties in the other parameters dependent on those by means of the Taylor series method of error propagation.

| $M_\infty$ | $Re_\ell \times 10^{-6}$ | Uncertainty (±), percent | | |
|------|------|------|------|------|
| | | $P_o$ | $T_o$ | $Re_\ell$ |
| 7.90 | 2.2 | 0.5 | 0.4 | 1.2 |
| 7.93 | 3.2 | 0.3 | | |
| 7.94 | 3.4 | 0.3 | | |
| 7.94 | 4.3 | 0.2 | | |
| 7.95 | 5.4 | 0.2 | | 1.1 |
| 7.96 | 6.5 | 0.2 | | |
| 7.97 | 7.5 | 0.1 | | |
| 7.98 | 8.6 | | | |
| 7.98 | 9.7 | | | |
| 7.99 | 10.8 | | | |
| 7.99 | 11.9 | | | |
| 7.99 | 12.9 | | | |
| 8.00 | 14.0 | | | |
| 8.00 | 15.1 | | | |

## 4.2 DATA

Infrared camera calibrations are repeatable within ±1 percent in absolute temperature and are within ±1 percent of the calibration supplied by the camera manufacturer. Initial model surface temperature, measured with a thermocouple probe which was checked periodically, is estimated to be ±0.5 percent of reading, °F. Model angle of attack is estimated to have an uncertainty of ±0.2 deg.

The overall estimated uncertainty in the heat-transfer coefficients is as follows:

| $h(T_o)$ | Uncertainty (±), percent |
|------|------|
| $10^{-3}$ | 12 |
| $10^{-2}$ | 7 |

These values were based on the following assumptions:

| Item | Estimated Uncertainty ($\pm$), percent |
|------|----------------------------------------|
| k | 5 |
| $C_p$ | 5 |
| $\rho$ | 1 |
| $T_i$ | 0.5 |
| $T_w$ | 1 |
| $T_o$ | 0.4 |
| t | 1 |

## 5.0 RESULTS AND DISCUSSION

### 5.1 GENERAL

The influence of simulated thermal protection tiles on the heat-transfer distribution of the Orbiter windward surface is obviously an extremely complex subject. This section will illustrate the general character of the heating patterns, and examples of the heating level and distribution along the model centerline will be presented. A complete study and correlation of the results as they apply towards specifying allowable full-scale tile roughness will be performed by Rockwell International.

A color photograph presented in Fig. 12 is typical of the monitor video display viewed during the test. Reference temperatures corresponding to the interface between colors are shown along the color bar at the bottom of the photograph. As has been stated earlier, when the model properties and run time are known, the color interface lines can be reduced to heat-transfer coefficient if required. Additional points of interest are noted on the photograph. All other photographs included in this report are black and white prints made from color negatives. This yields ten distinct shades of gray which will serve to show the major areas of interest in the heating patterns. Note that the mirror in the viewing path reverses the video screen scene and photographs left-to-right.

## 5.2 TILE HEIGHT EFFECTS

Before discussing heat-transfer distributions, it should be useful to compare the thickness of a laminar boundary layer at the tile stations with the range of the tile heights tested. Figure 13 shows the boundary-layer thickness at the tile stations at both 30- and 40-deg angle of attack. Calculations were performed assuming a wall temperature of 560°R forward of the tile station which seems reasonable in light of the typical temperature distributions illustrated in Fig. 14. These calculations as well as the theoretical heat-transfer values presented in later figures were performed by simulating the windward centerline of the Orbiter with a hyperboloid and following the methods described in Refs. 6 through 8. Additional information on the hyperboloid simulation is available in Ref. 9. The primary observation to be made from Fig. 13 is that the tile height was always less than the calculated local laminar boundary-layer thickness.

Tile height influences on windward longitudinal centerline heat-transfer distribution at $Re_\ell = 6.5 \times 10^6$ and $\alpha = 30$ deg are shown in Fig. 15a. These data show an orderly forward movement of transition with increasing tile height. Figure 15b illustrates similar results on Configuration 7 (tile $x/\ell = 0.111$) with the addition of the cavity tile setting, -0.020 in. These data indicate that the cavity had no more influence than the zero height setting with the same 0.010-in. gap setting. The photographs in Fig. 16 illustrate the overall view of the windward surface heating pattern with variations in tile height at $Re_\ell = 6.5 \times 10^6$ at $\alpha = 30$ deg. These photographs show the development of the wedge-shaped transitional and turbulent region typical of delta wing configurations. This region moved forward with increasing tile height until it reached a position immediately downstream of the center tile.

## 5.3 AXIAL TILE LOCATION EFFECTS

Figure 17a shows the centerline heat-transfer distribution at $Re_\ell = 6.5 \times 10^6$ and $\alpha = 30$ deg with a tile height of 0.010 in. These data indicate that the boundary-layer tripping effectiveness decreased as the tile station was moved aft and the tiles were submerged in a thicker boundary layer (see Fig. 13). When the Reynolds number was increased to $8.6 \times 10^6$, a 0.010-in. tile setting was sufficient to produce fully turbulent heating aft of each tile station as shown in Fig. 17b.

Photographs in Fig. 18 show the distinct character of the heating distributions which result when the tile axial location is changed. When the tiles were located at $x/\ell = 0.050$ (Configuration 6, Fig. 18a), the laminar zones between the tile clusters very rapidly turn outboard and sweep over the leading edge. Moving the tiles aft (Figs. 18b and c) resulted in two clear laminar zones which generally extended aft from the space between the tile clusters. The large asymmetry in Fig. 18c (Configuration 8, tile $x/\ell = 0.175$) is caused by the asymmetric lateral placement of the outboard tile clusters. Note that only Configuration 8 has asymmetric outboard tile locations (see Fig. 6).

## 5.4 TILE GAP EFFECTS

The influence of gap variation with a constant tile height is shown in Figs. 19 and 20. Figure 19a illustrates data from Configuration 6 (tile $x/\ell = 0.050$) for $Re_\ell = 7.5 \times 10^6$ at $\alpha = 30$ deg. These data show a significant influence of gap size on heat transfer downstream of the tile cluster. Data in Fig. 19b indicate that gap variation had no influence when the tiles were located at $x/\ell = 0.175$. However, the gap variation tests for Configuration 8 (tile $x/\ell = 0.175$) were performed with a tile height of 0.015 in. The data indicate that turbulent heating existed with a zero gap. Consequently, these cases may have been dominated by the tile height although it might be expected that gap change effects would not be significant because of the thicker boundary layer at the aft station. It should be noted that only the gap around the adjustable tiles was changed for the 0.020-in. case, while all other gaps were 0.010 in. For the zero gap case, all gaps were filled.

The photographs in Fig. 20 show the forward movement and overall enlargement of the transitional and turbulent zone with increased gap size.

## 5.5 REYNOLDS NUMBER EFFECTS

Variation in the longitudinal centerline heat-transfer distribution with changes in free-stream Reynolds number is shown in Fig. 21. Then data were obtained on Configuration 6 (tile $x/\ell = 0.050$) with the tile height set at 0.010 in. At $Re_\ell = 4.3 \times 10^6$, the distribution is in very good agreement with theoretical values and with data from a smooth wall thin-skin model (Ref. 3). As expected, increasing free-stream Reynolds number brought transition forward on the body.

Corresponding photographs in Fig. 22 show changes in the overall heating pattern. The increase in the transitional and turbulent zones is evident as Reynolds number was increased. Note the increased asymmetry at $Re_\ell = 10.8 \times 10^6$. Figure 6 shows that the projecting center tile is not on the centerline of the model but is displaced to the left. Any influence on the heating distribution would appear on the right side of the photographs as is the case in Fig. 22c. It was indicated earlier that the photographs are reversed left to right because of the mirror in the viewing system.

Additional photographs in Fig. 23 show the heating distributions on Configuration 7 with variation in Reynolds number. Reynolds number influence is clearly evident in the reduction of the length of the laminar streaks between the tile clusters as Reynolds number was increased.

## 5.6 ANGLE-OF-ATTACK EFFECTS

Two examples of angle-of-attack influences on centerline heat-transfer distributions are shown in Figs. 24. Figure 24a illustrates data obtained with the tile height at zero and all gaps at 0.010 in. These data show that a large region of transitional heating existed on the model at $\alpha$ = 30 deg and $Re_\ell = 8.6 \times 10^6$. When the angle of attack was increased to 40 deg, the onset of transition moved forward and the heating level increased. Figure 24b illustrates a case in which a well-developed turbulent heating distribution existed at $\alpha$ = 30 deg with the tile height and gaps at 0.010 in. Increasing angle of attack from 30 to 40 deg did not change the character of the distribution, but the level increased significantly.

Heating distribution photographs in Figs. 25 and 26 show variations in overall heating distributions for Configurations 6 and 7, respectively. Figure 26 shows the forward progress and enlargement of the high heating area as angle of attack increased with the tiles at zero height. With the tiles at 0.010 in. (Fig. 26), the crossflow increase is evident from observing the change in the low heating streak shapes with increasing angle of attack.

## 5.7 TRIP EFFECTIVENESS

An example of a summary of tile effectiveness as a boundary-layer trip is illustrated in Fig. 27. The end of transition was determined from the windward centerline heat-transfer distributions as

indicated on the sketch included on Fig. 27. When compared to the smooth-wall transition case from Ref. 1, the tile is a very effective trip. These data give an indication of the forward progress of the front of the wedge-shaped turbulent zone on the model and must be evaluated in the light of the overall heating distributions as shown in the photographs presented earlier. Uncertainty in the character of the effectiveness curve can be introduced by turbulent front asymmetry which developed in some runs because of the asymmetric lateral tile setting.

## 6.0 SUMMARY OF RESULTS

Examples of heat-transfer data obtained during tests of 0.040-scale models of the forward half of the Space Shuttle Orbiter Configuration 140C with simulated thermal protection tiles have been presented. A few general observations may be made based on the data and discussion presented:

1. An infrared scanning system was used to obtain heat-transfer data which were in good agreement with theoretical values and data obtained using the thin skin technique.

2. Projecting tiles were effective boundary-layer trips. Moving the tile station aft reduced the tile tripping effectiveness.

3. Increasing gap size increased heating downstream of the tile station when the tiles were located at $x/\ell = 0.050$. Data obtained for tile $x/\ell = 0.175$ indicated no gap influence.

4. Increasing free-stream Reynolds number moved transition forward along the longitudinal centerline. Off-centerline distributions indicated similar orderly trends as evidenced by the reduction of the length of laminar streaks between tile clusters.

5. An increase in angle of attack increased the heat-transfer level and the crossflow which changed the character of the heating distribution. Increasing angle of attack also tended to move transition forward.

## REFERENCES

1. Carver, D. B. "Heat-Transfer Tests on the Rockwell International Space Shuttle Orbiter with Boundary-Layer Trips." AEDC-TR-76-28

2. Sivells, James C. "Aerodynamic Design and Calibration of the VKF 50-Inch Hypersonic Wind Tunnels." AEDC-TDR-62-230 (AD299774), March 1963.

3. Carter, L. D. and Kaul, C. E. "Heat-Transfer Tests on the Rockwell International Space Shuttle Orbiter with and without Simulated Protuberances." AEDC-TR-75-20 (ADA012876), July 1975.

4. Bynum, D. S., Hube, F. K., Key, C. M., and Dyer, P. M. "Measurement and Mapping of Aerodynamic Heating in VKF Tunnel B with an Infrared Camera." AEDC-TR-76-54

5. Fay, J. A. and Riddell, F. R. "Theory of Stagnation Point Heat Transfer in Dissociated Air." Journal of Aerospace Sciences. Vol. 25, No. 2, February 1958, pp. 73-85, 121.

6. Patankar, S. V. and Spalding, D. B. Heat and Mass Transfer in Boundary Layers. CRC Press, Cleveland, 1968.

7. Mayne, A. W., Jr. and Dyer, D. F. "Comparisons of Theory and Experiment for Turbulent Boundary Layers on Simple Shapes at Hypersonic Conditions." Proceedings of the 1970 Heat Transfer and Fluid Mechanics Institute. Stanford University Press, 1970.

8. Inouye, M., Rakich, J. V., and Lomax, H. "A Description of Numerical Methods and Computer Programs for Two-Dimensional and Axisymmetric Supersonic Flow over Blunt-Nosed and Flared Bodies." NASA TN D-2970, August 1965.

9. Adams, J. C., Jr., Martindale, W. R., Mayne, A. W., and Marchand, E. O. "Real Gas Scale Effects on Hypersonic Laminar Boundary-Layer Parameters Including Effects of Entropy-Layer Swallowing." AEDC-TR-75-2 (ADA018755), December 1975.
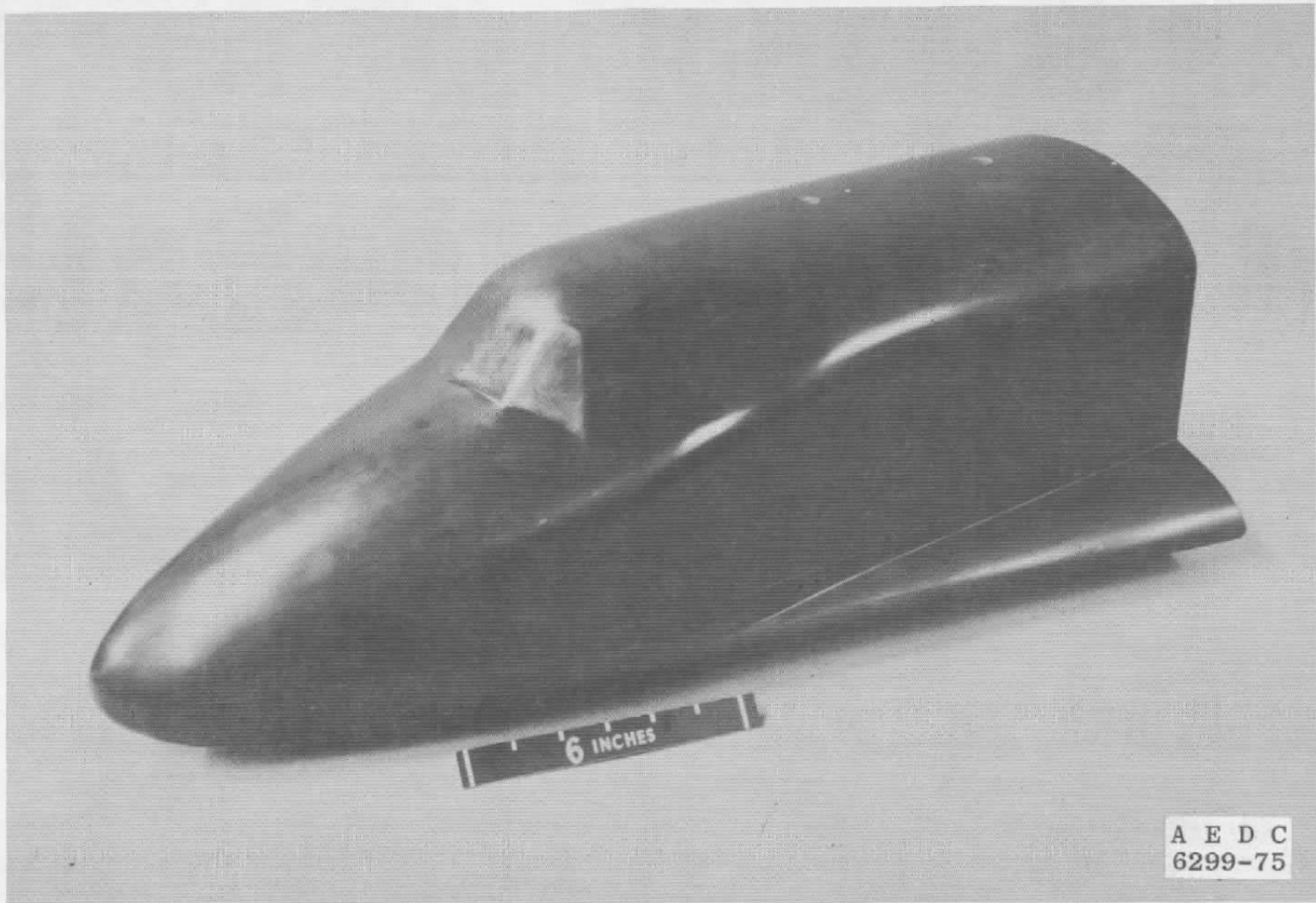
6 INCHES

AEDC
6299-75

Figure 1. Photograph of Orbiter Forebody Model.

13.2

9.2

$\ell/2 = 25.87$

x

*⑥  *⑦  *⑧

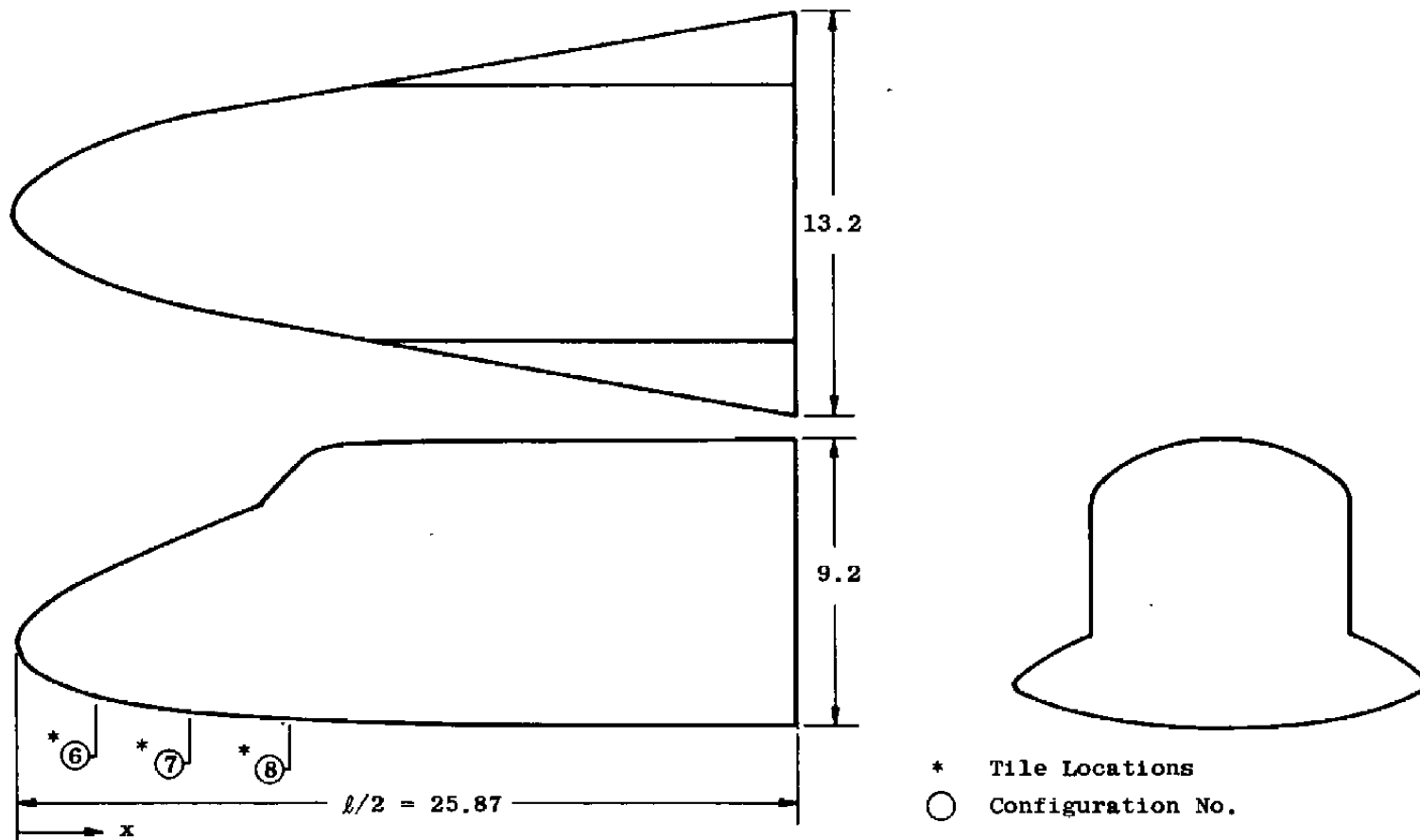\*  Tile Locations

◯  Configuration No.
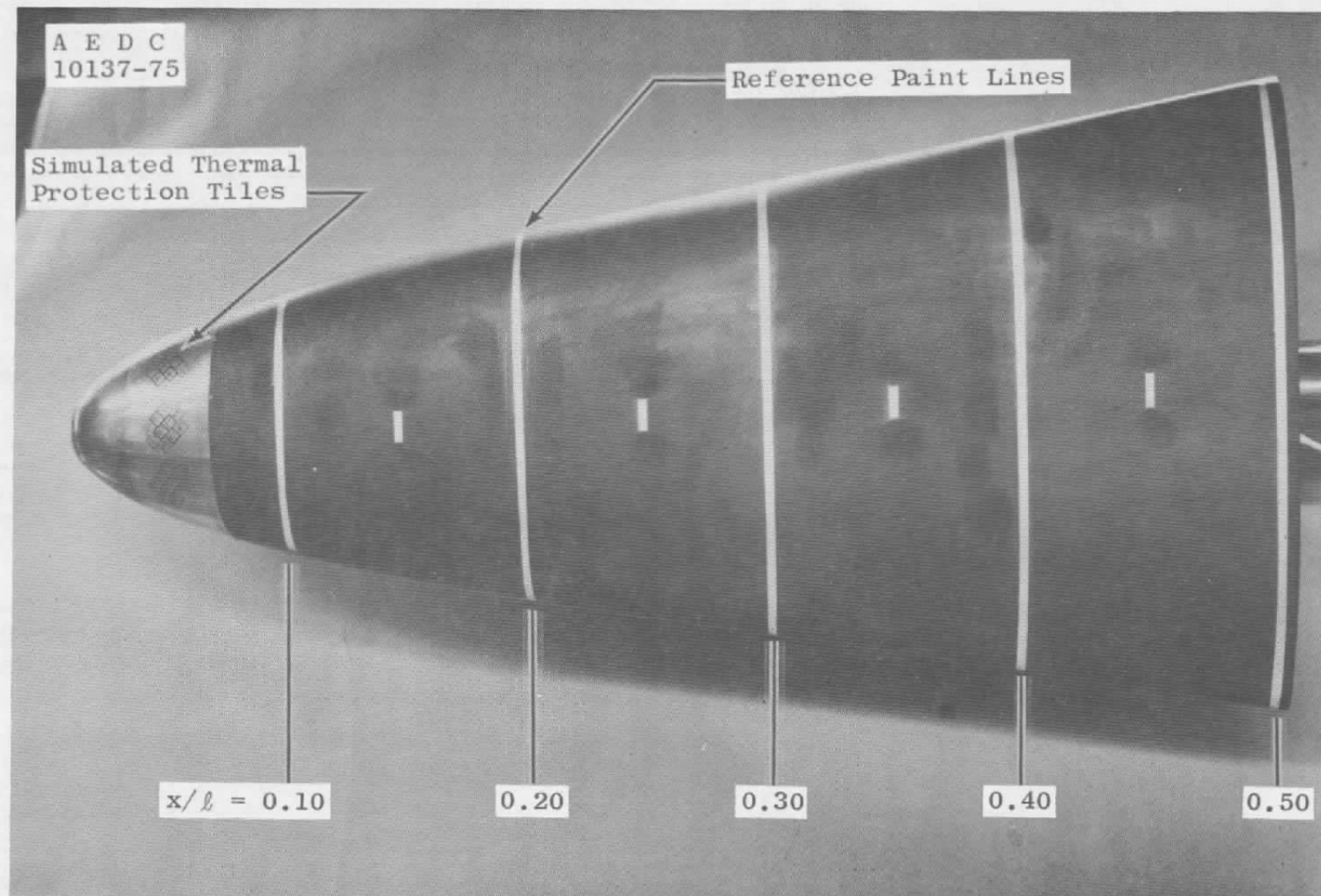
Figure 2.  Overall model geometry.

Figure 3. Photograph of Orbiter lower surface, Configuration 6.
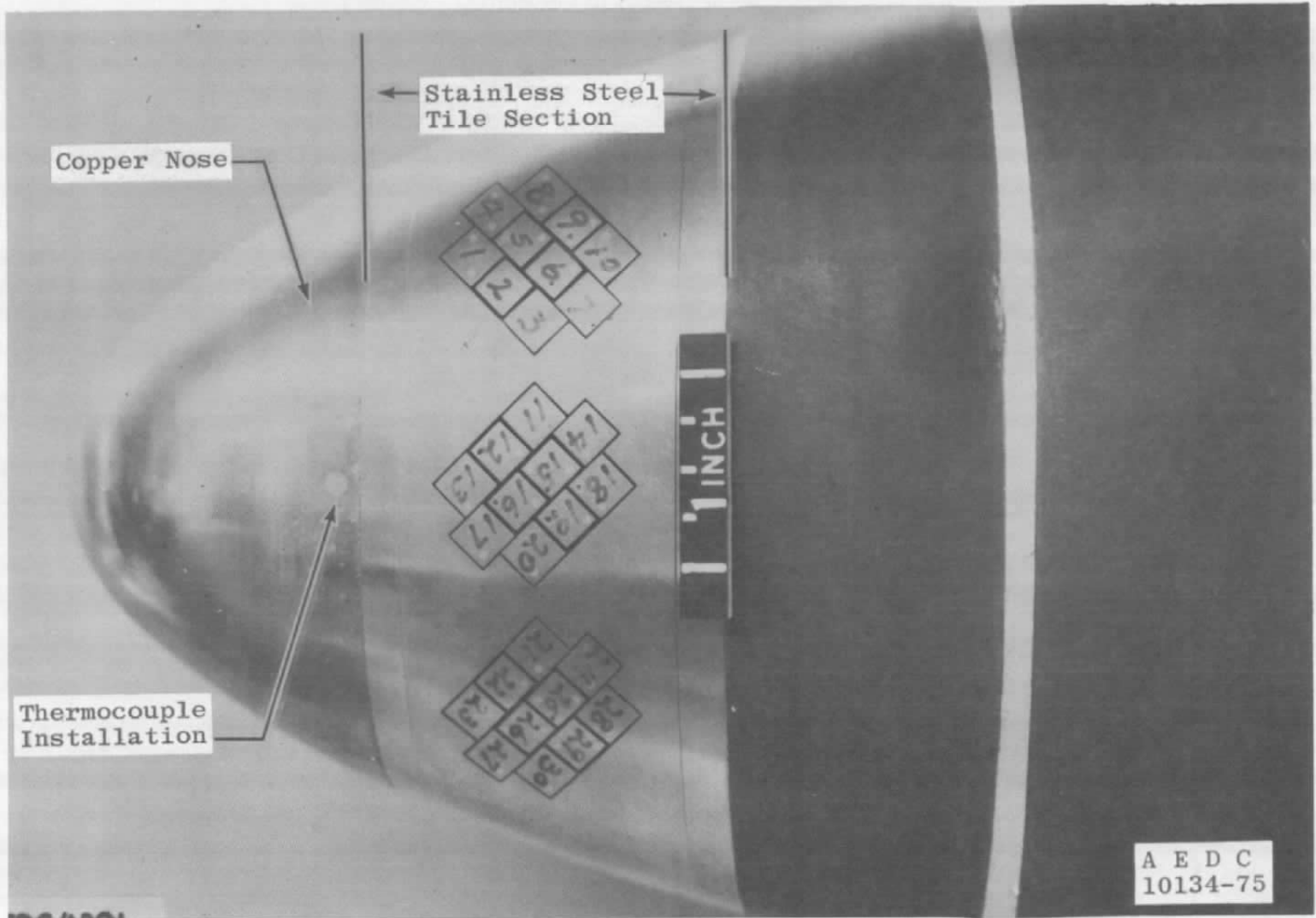
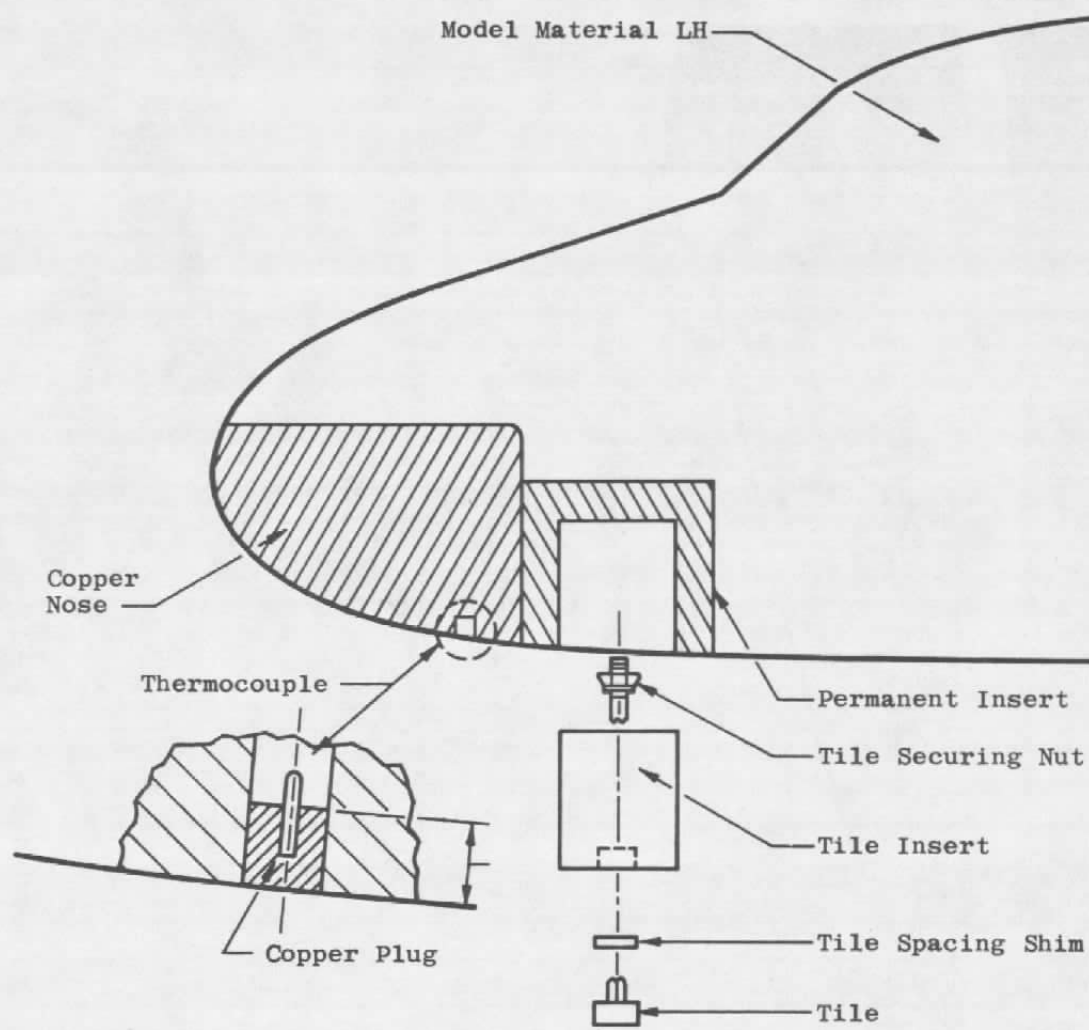Figure 4. Photograph of simulated thermal protection tile installation, Configuration 6.
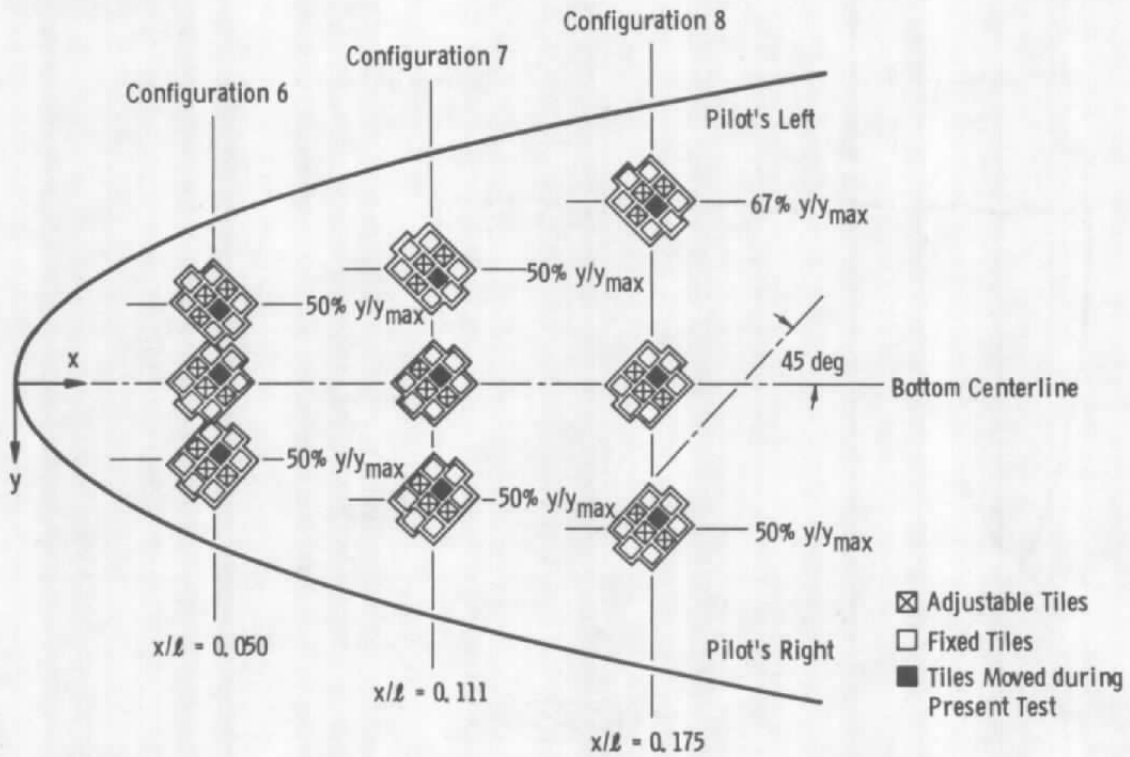
Model Material LH

Copper
Nose

Thermocouple

Copper Plug

Permanent Insert

Tile Securing Nut

Tile Insert

Tile Spacing Shim

Tile

Figure 5.  Tile installation details.

Figure 6. Tile cluster locations.
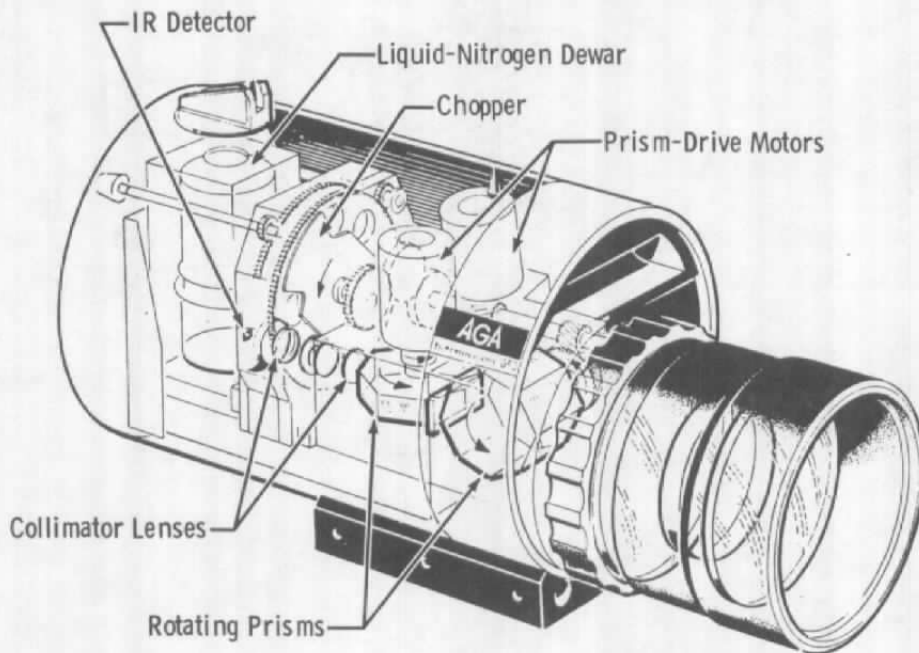


Figure 7. Infrared scanning camera.
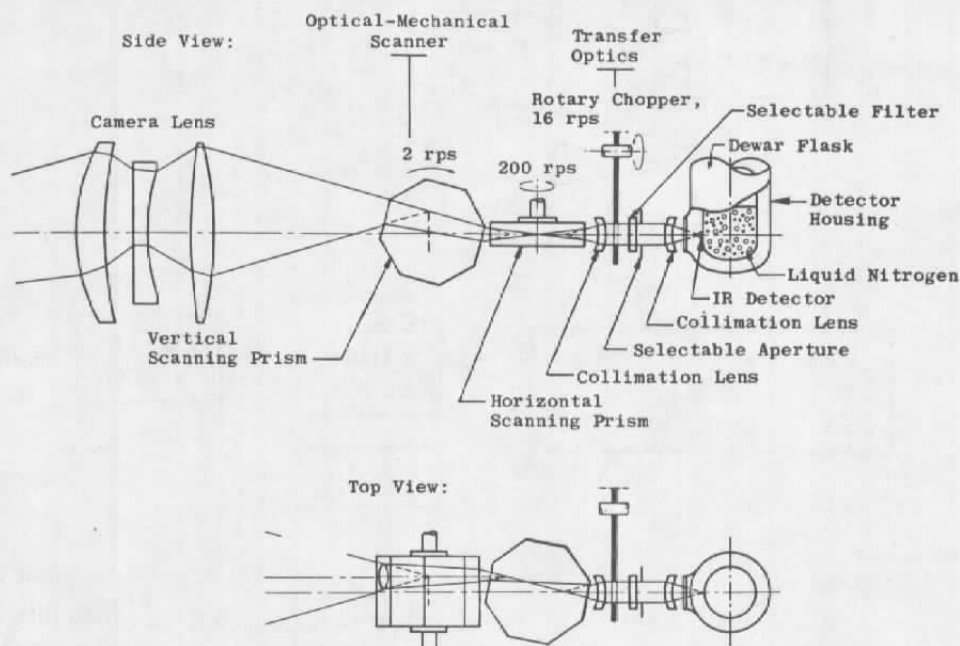
Side View:

Optical-Mechanical
Scanner

Transfer
Optics

Rotary Chopper,
16 rps

Camera Lens

Selectable Filter

Dewar Flask

2 rps

200 rps

Detector
Housing

Liquid Nitrogen

IR Detector

Collimation Lens

Selectable Aperture

Vertical
Scanning Prism

Collimation Lens

Horizontal
Scanning Prism

Top View:

Figure 8.  Infrared scanning camera internal layout.

45
deg

Irtran Window

Infrared Camera

Front Surfaced Mirror

Camera Location

| Test Entry | A, in. |
|---|---|
| 1 | 48.75 |
| 2 | 38.00 |

A

50.0

Copper Block
Ref. Target

Notes:  1.  Not to Scale
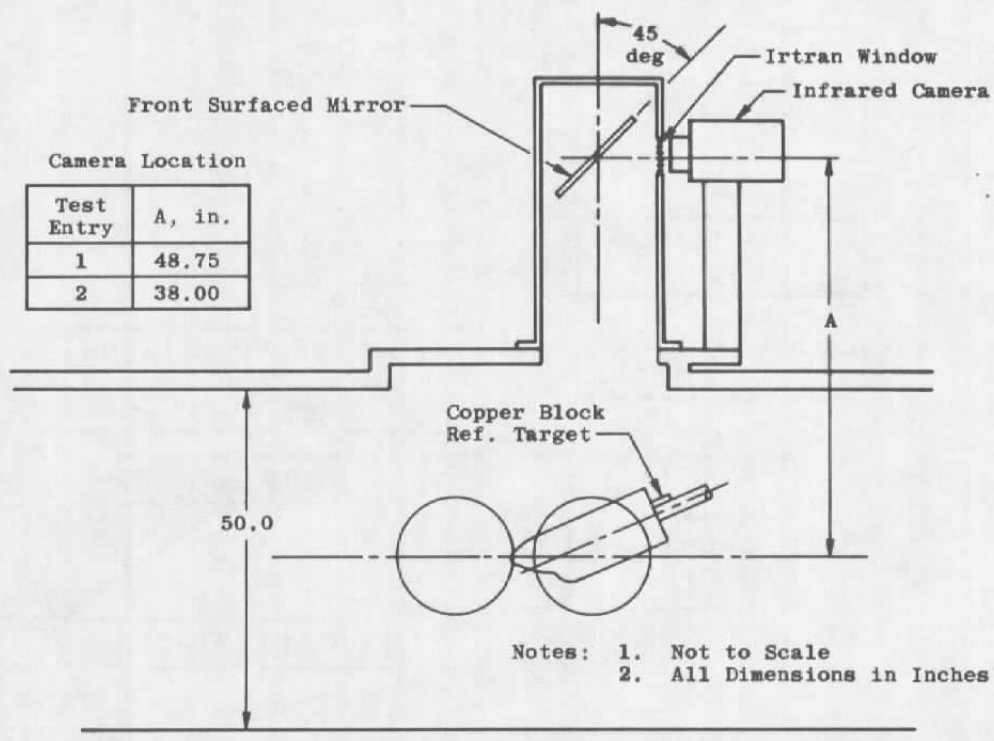        2.  All Dimensions in Inches
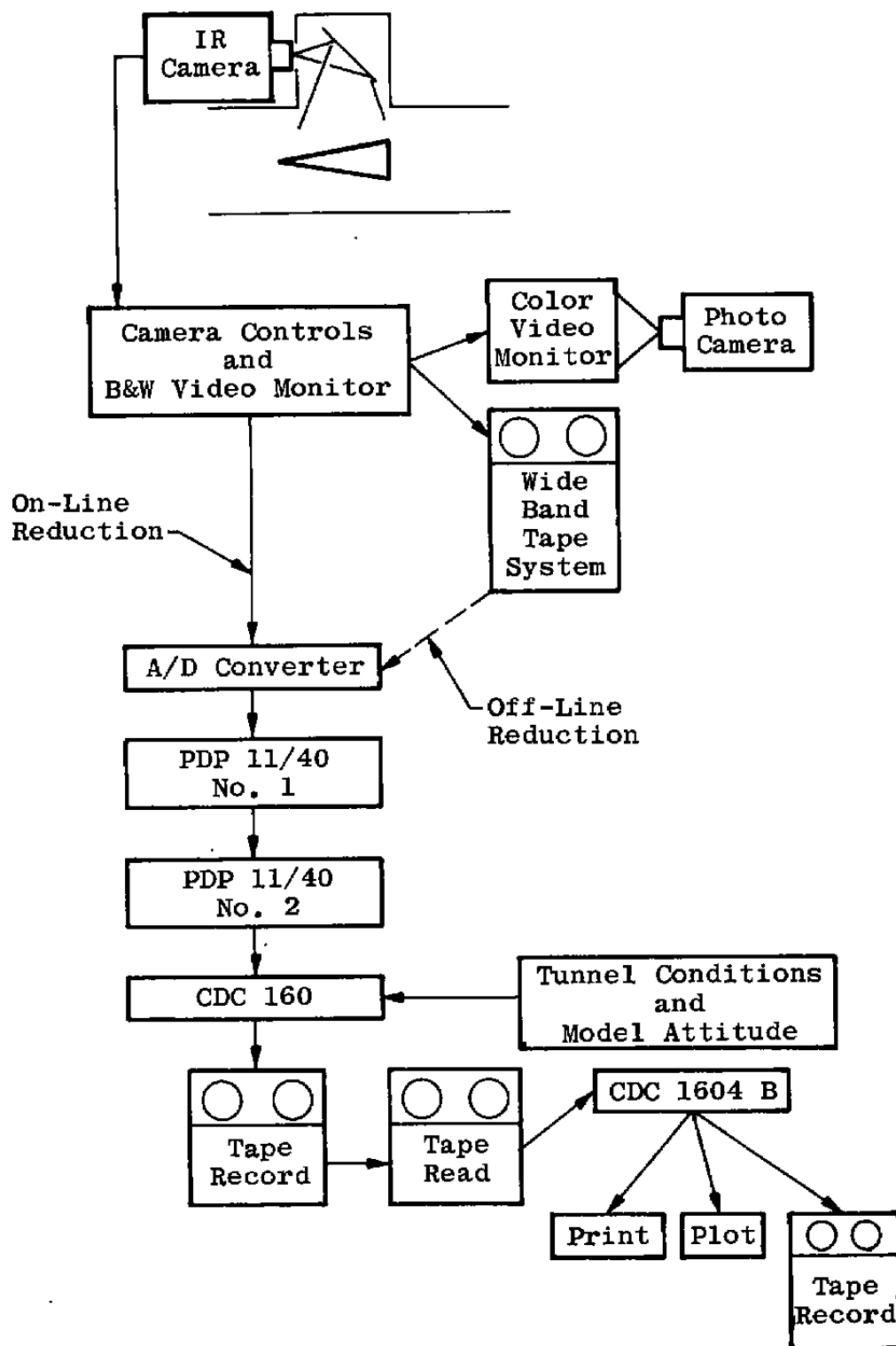
Figure 9.  Schematic of model and camera installation.

27

Figure 10. Infrared scanning data system schematic.
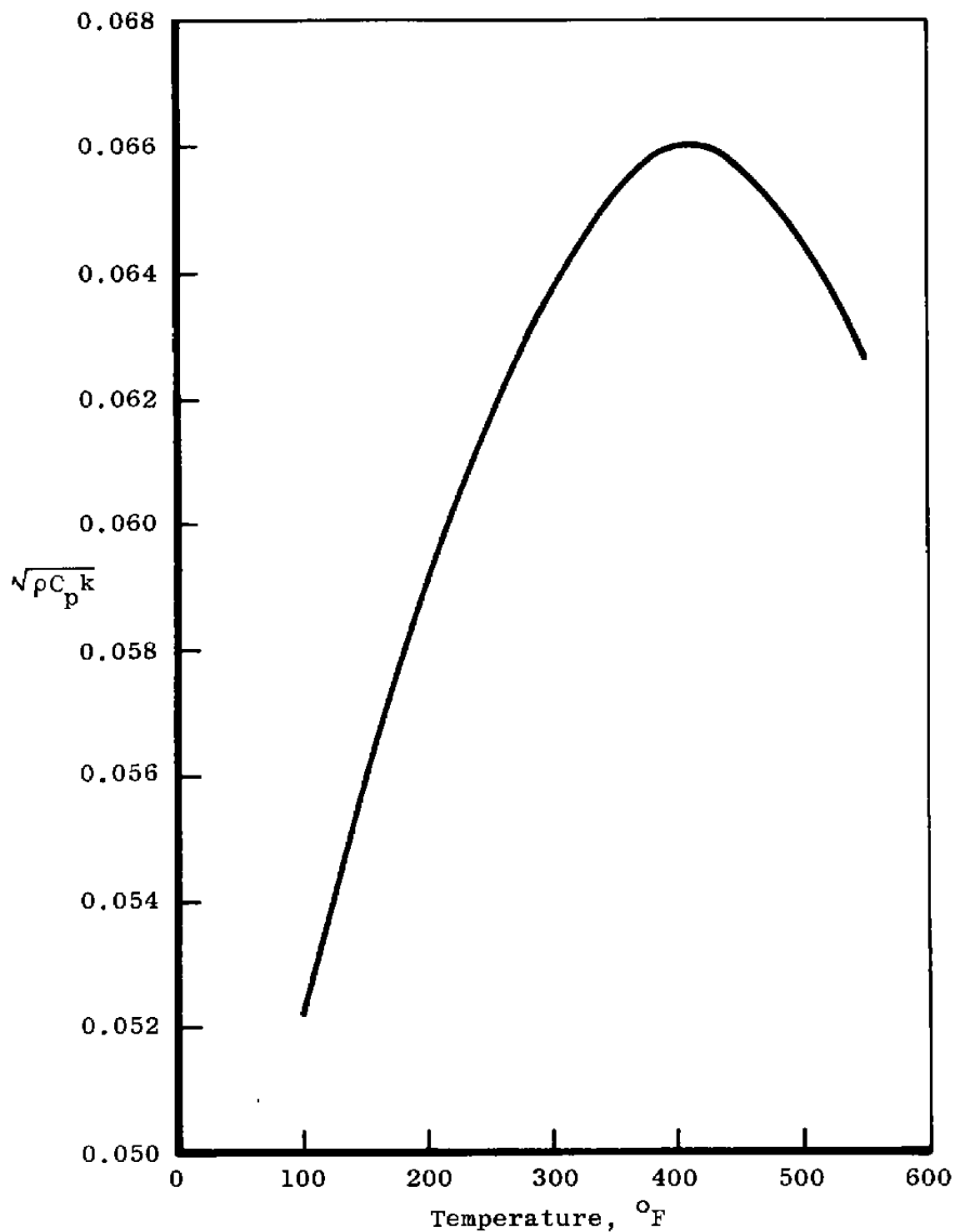
Figure 11.  Material properties of Lockheed Proprietary Material "LH."
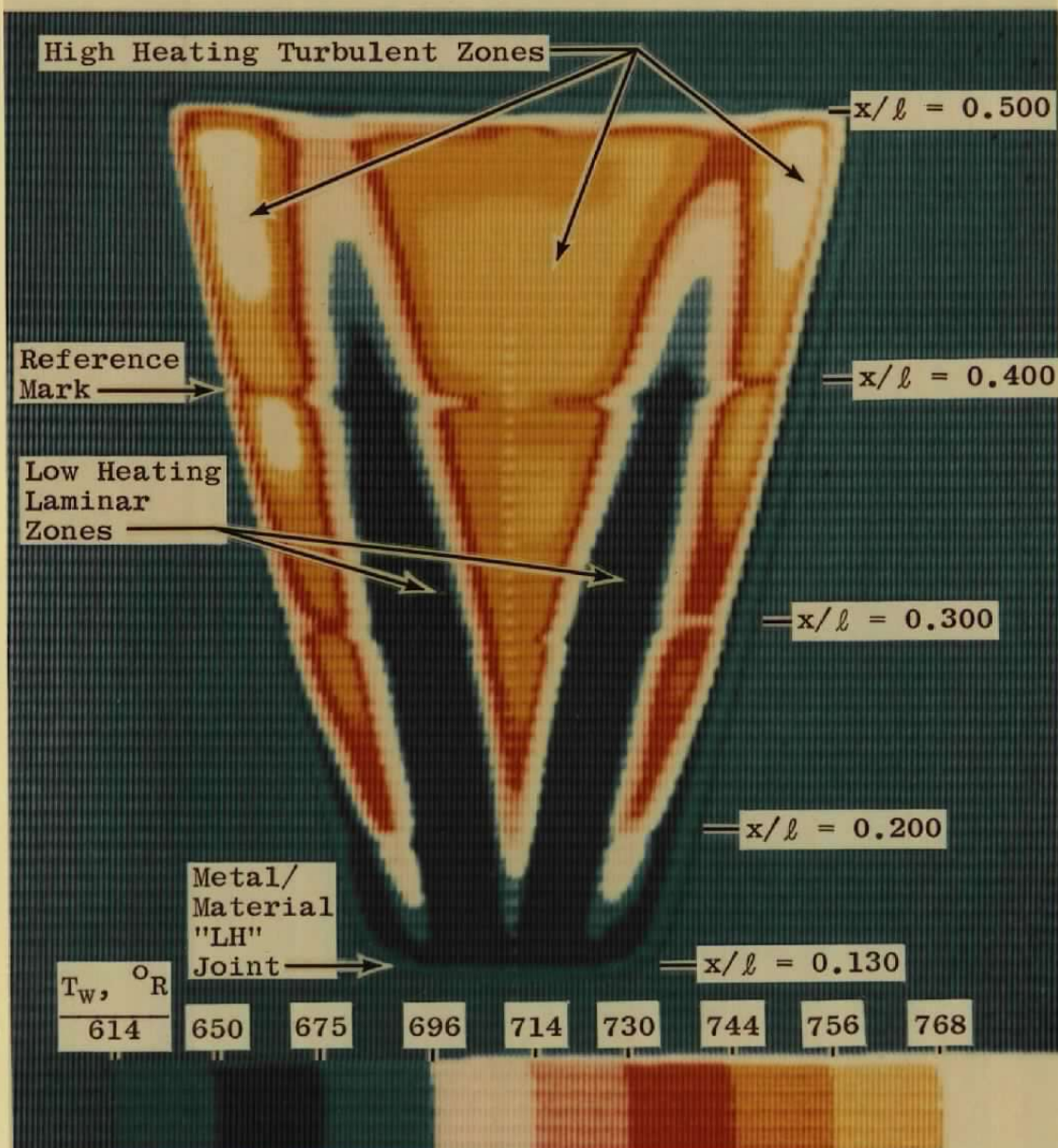
Figure 12. Representative photograph of the infrared system color video monitor.

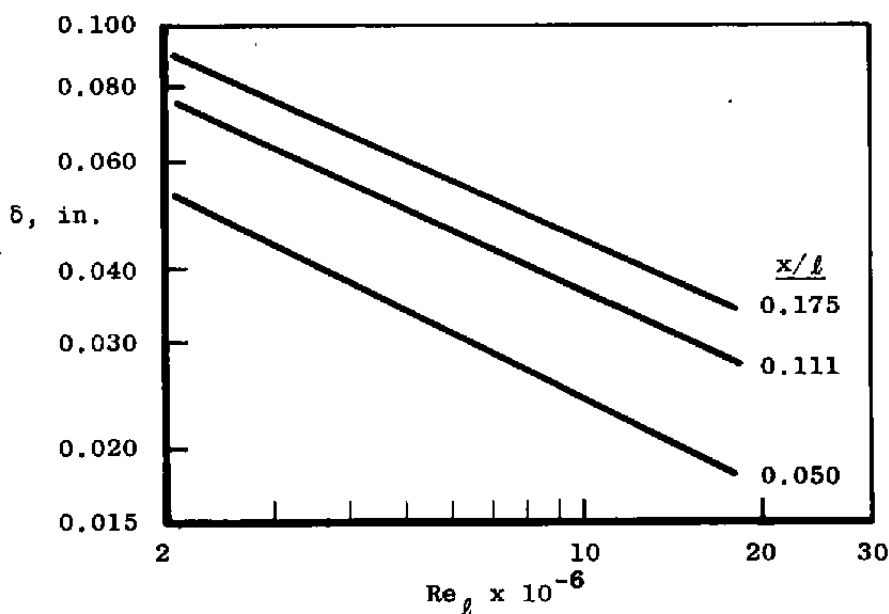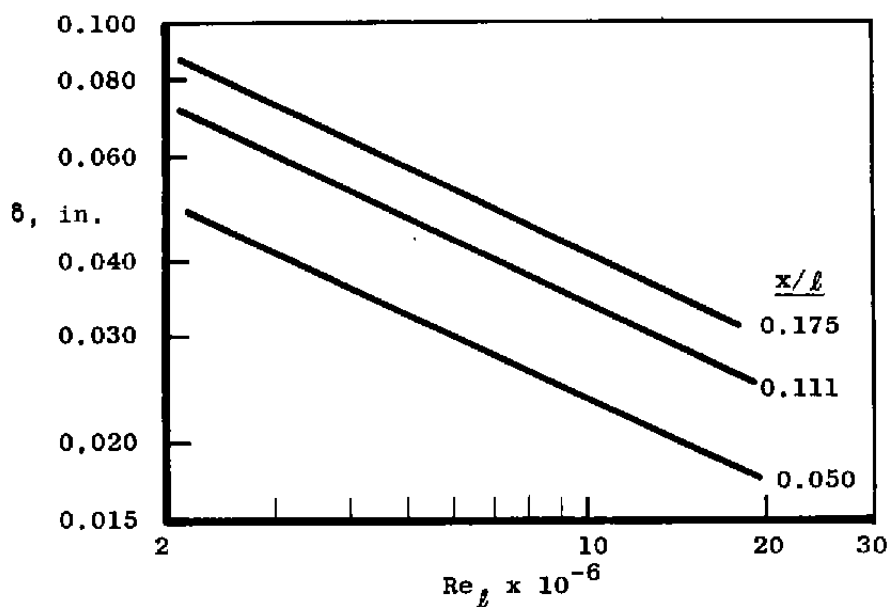| Config. | Tile Location, $x/\ell$ | Tile Height Range, in. |
|---------|--------------------------|-------------------------|
| 6 | 0.050 | -0.020 to 0.015 |
| 7 | 0.111 | -0.020 to 0.020 |
| 8 | 0.175 | -0.020 to 0.025 |

a. $a = 30$ deg

b. $a = 40$ deg

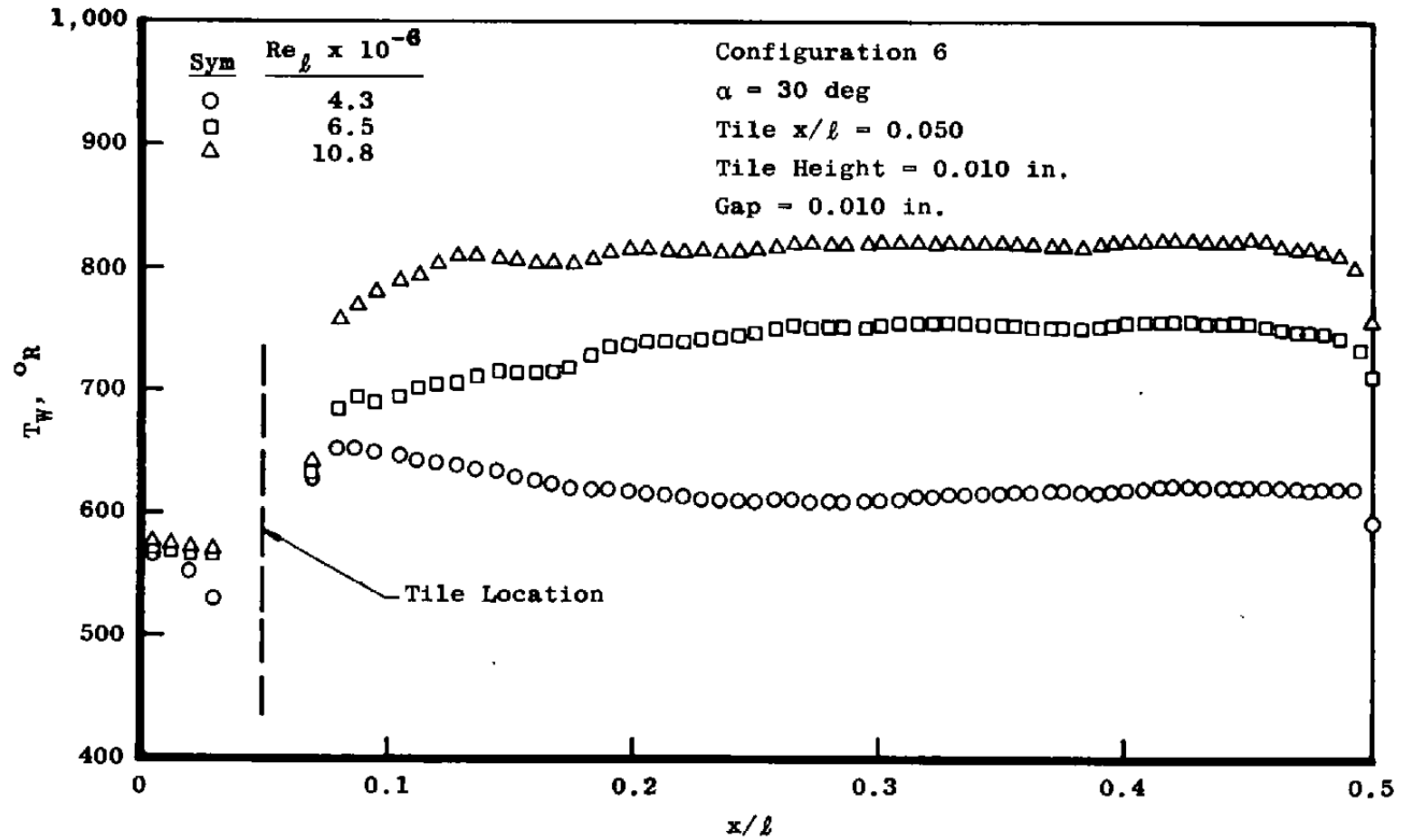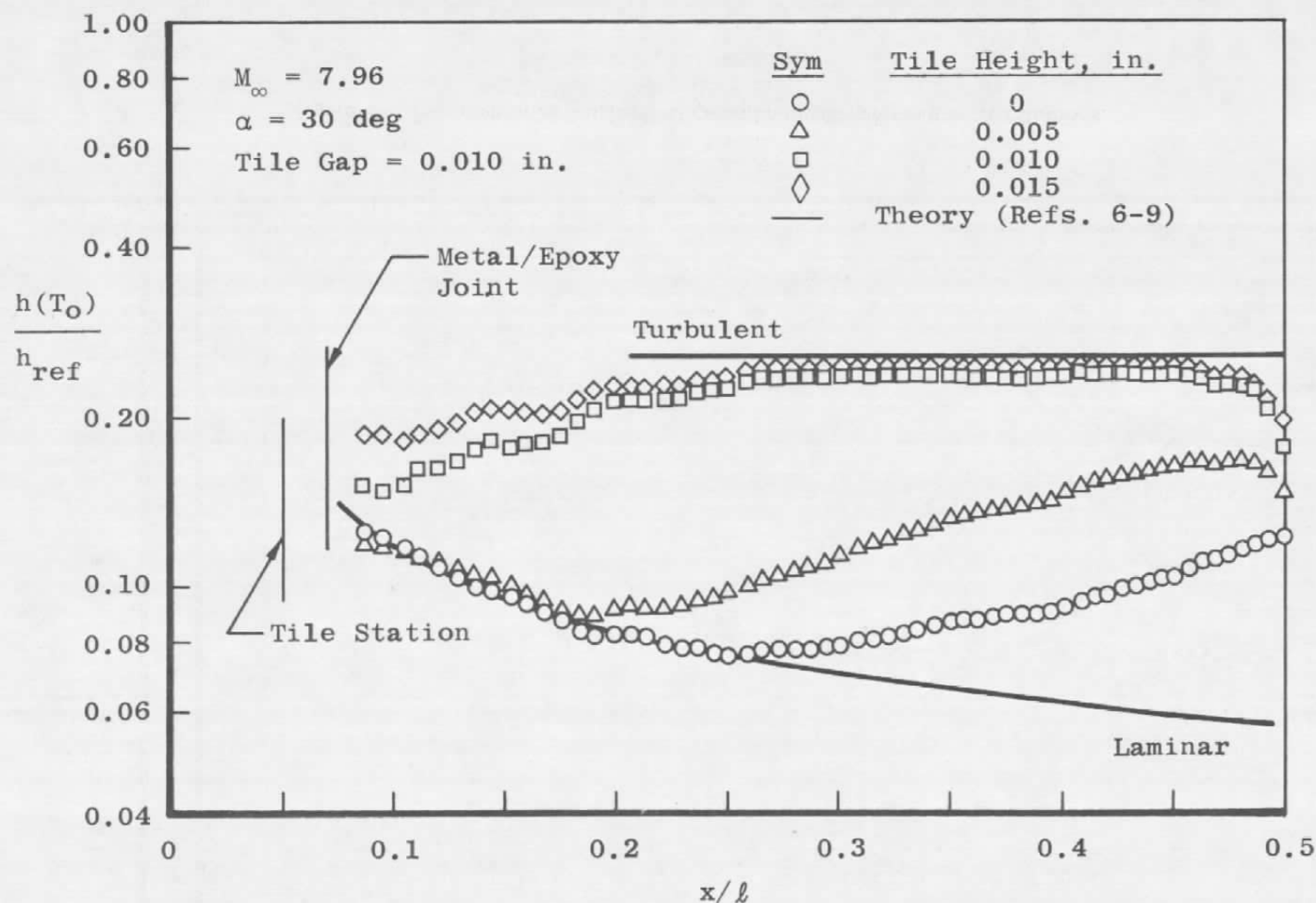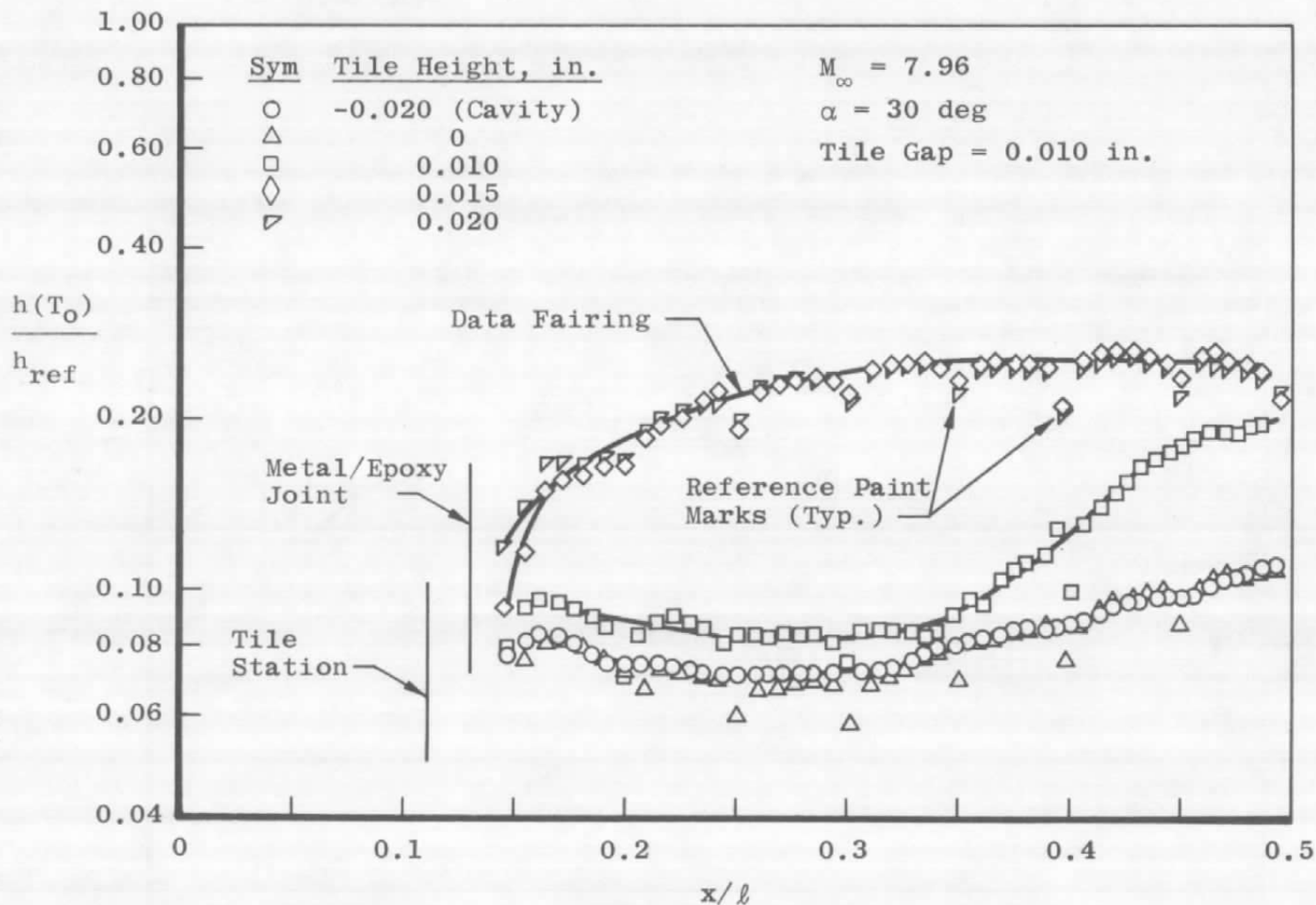Figure 13. Calculated boundary-layer thickness at the simulated tile locations.

Figure 14. Representative longitudinal centerline wall temperature distributions.

a. Configuration 6, tile x/ℓ = 0.050

Figure 15. Tile height influence on longitudinal windward centerline heat-transfer distribution at $Re_\ell = 6.5 \times 10^6$.

b. Configuration 7, tile $x/\ell$ = 0.111
Figure 15. Concluded.
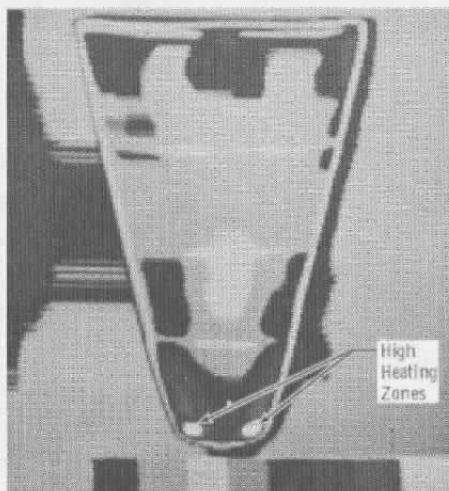
$M_\infty = 7.96$
Configuration 6
Tile $x/\ell = 0.050$
Tile Gap = 0.010 in.

a.  Tile height = 0

b.  Tile height = 0.005 in.
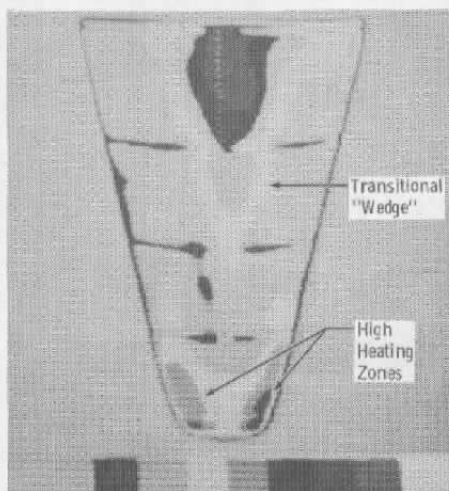
c.  Tile height = 0.015 in.

Figure 16.  Photographs of windward surface temperature distributions with tile height variation at $Re_\ell = 6.5 \times 10^6$, $a = 30$ deg.

a. $Re_\ell = 6.5 \times 10^6$

Figure 17. Tile axial location influence on longitudinal windward centerline heat-transfer distribution at $a = 30$ deg.
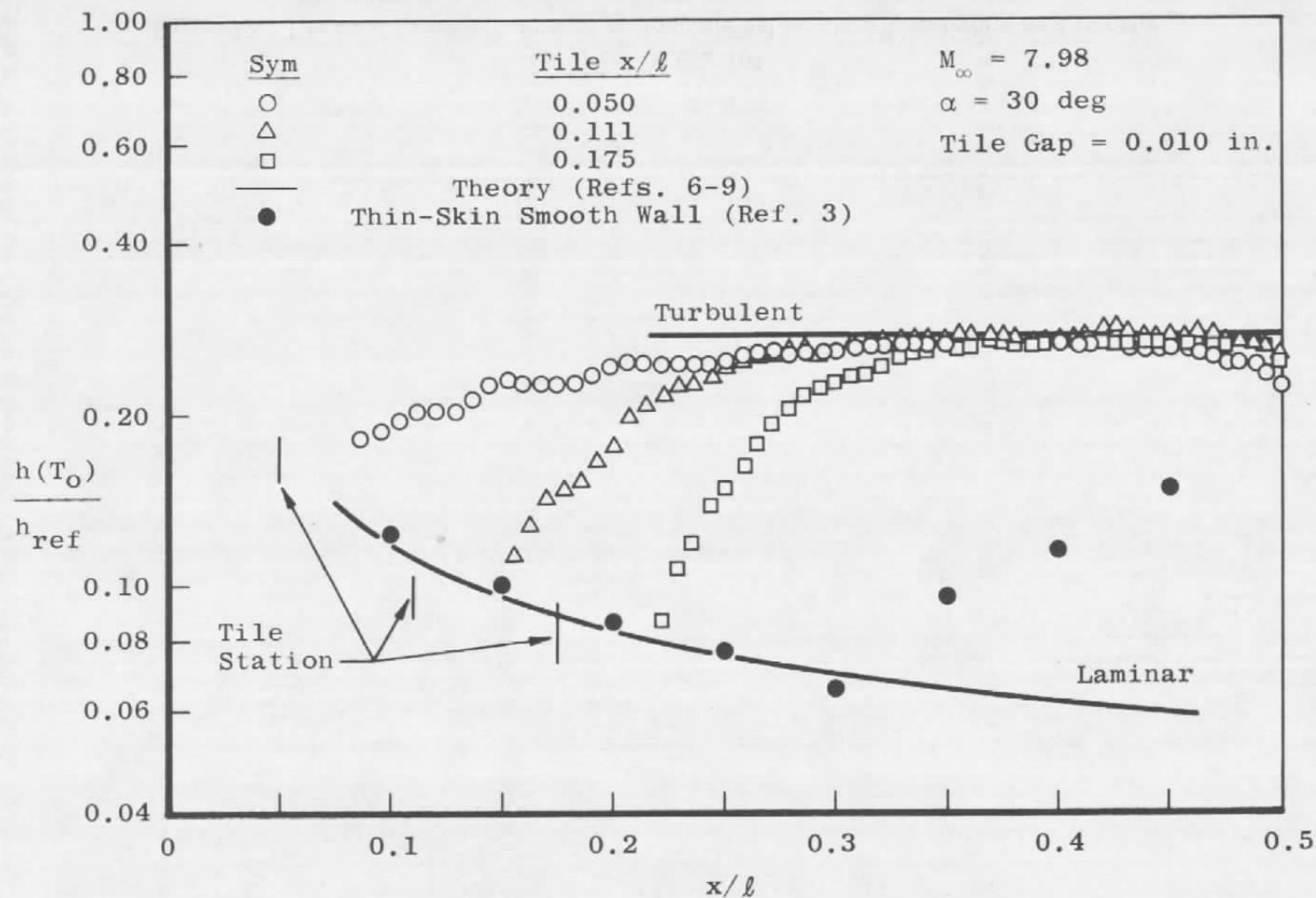
b. $Re_\ell = 8.6 \times 10^6$

Figure 17. Concluded.
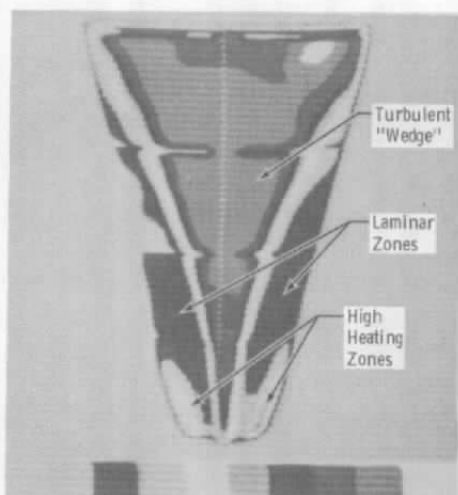
$M_\infty = 7.98$
Tile Height = 0.010 in.
Tile Gap = 0.010 in.

a. Configuration 6, tile $x/\ell = 0.050$
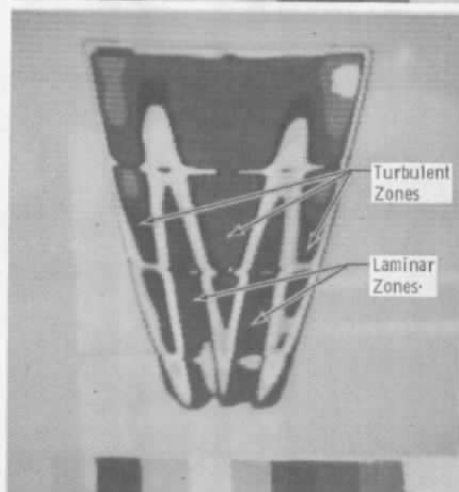
b. Configuration 7, tile $x/\ell = 0.111$
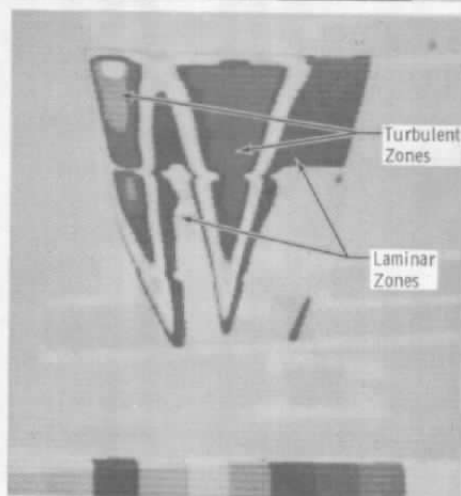
c. Configuration 8, tile $x/\ell = 0.175$

Figure 18. Photographs of windward surface temperature distribution with tile axial location variation at $Re_\ell = 8.6 \times 10^6$, $\alpha = 30$ deg.
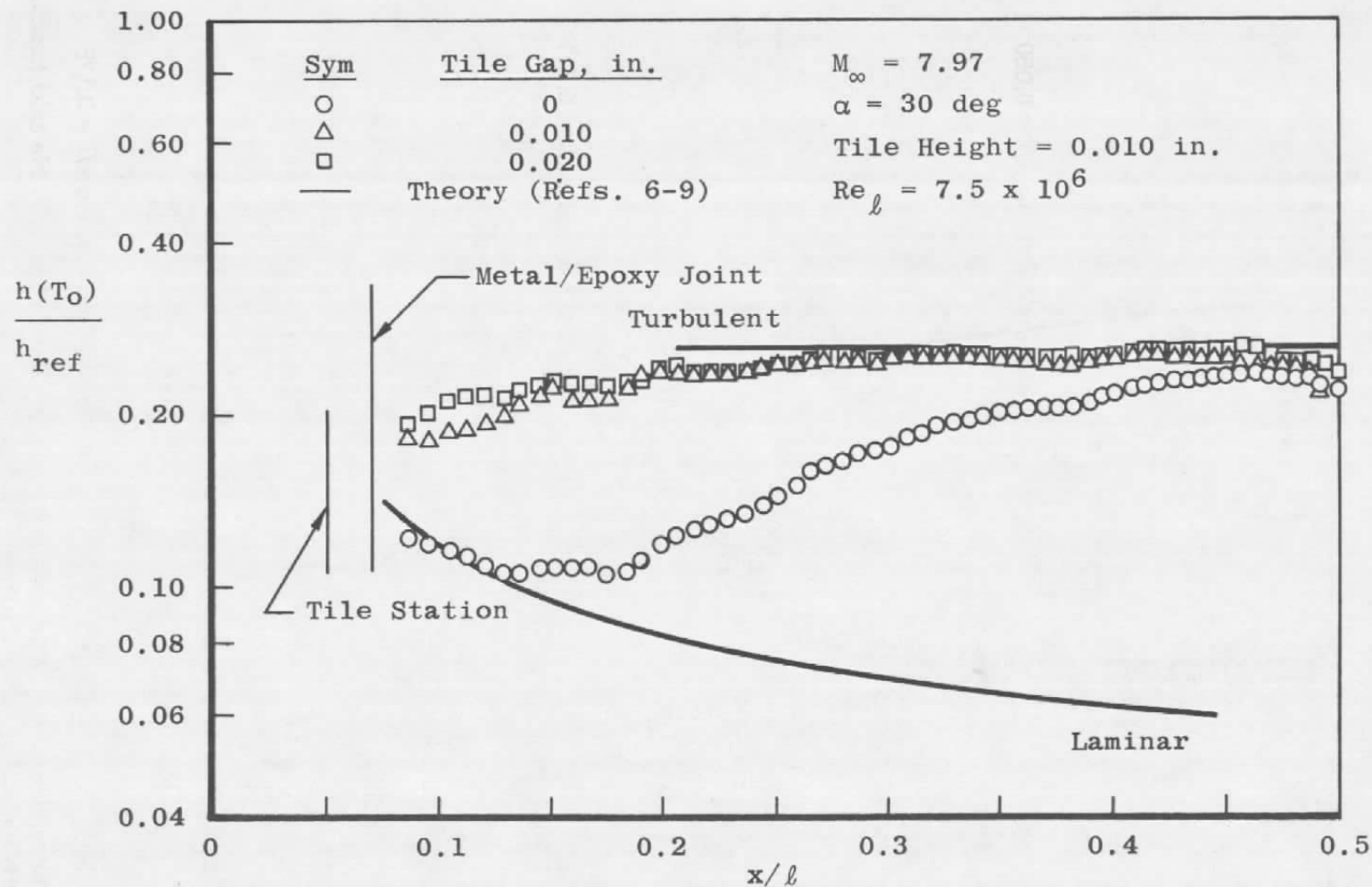
a. Configuration 6, tile x/ℓ = 0.050

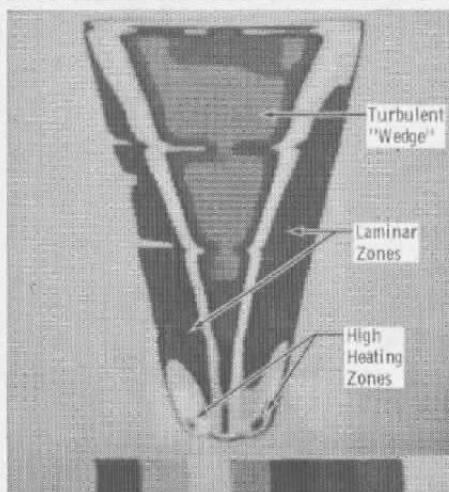Figure 19. Tile gap influence on longitudinal windward centerline heat-transfer distribution at $a$ = 30 deg, Re$_\ell$ = 7.5 x 10$^6$.
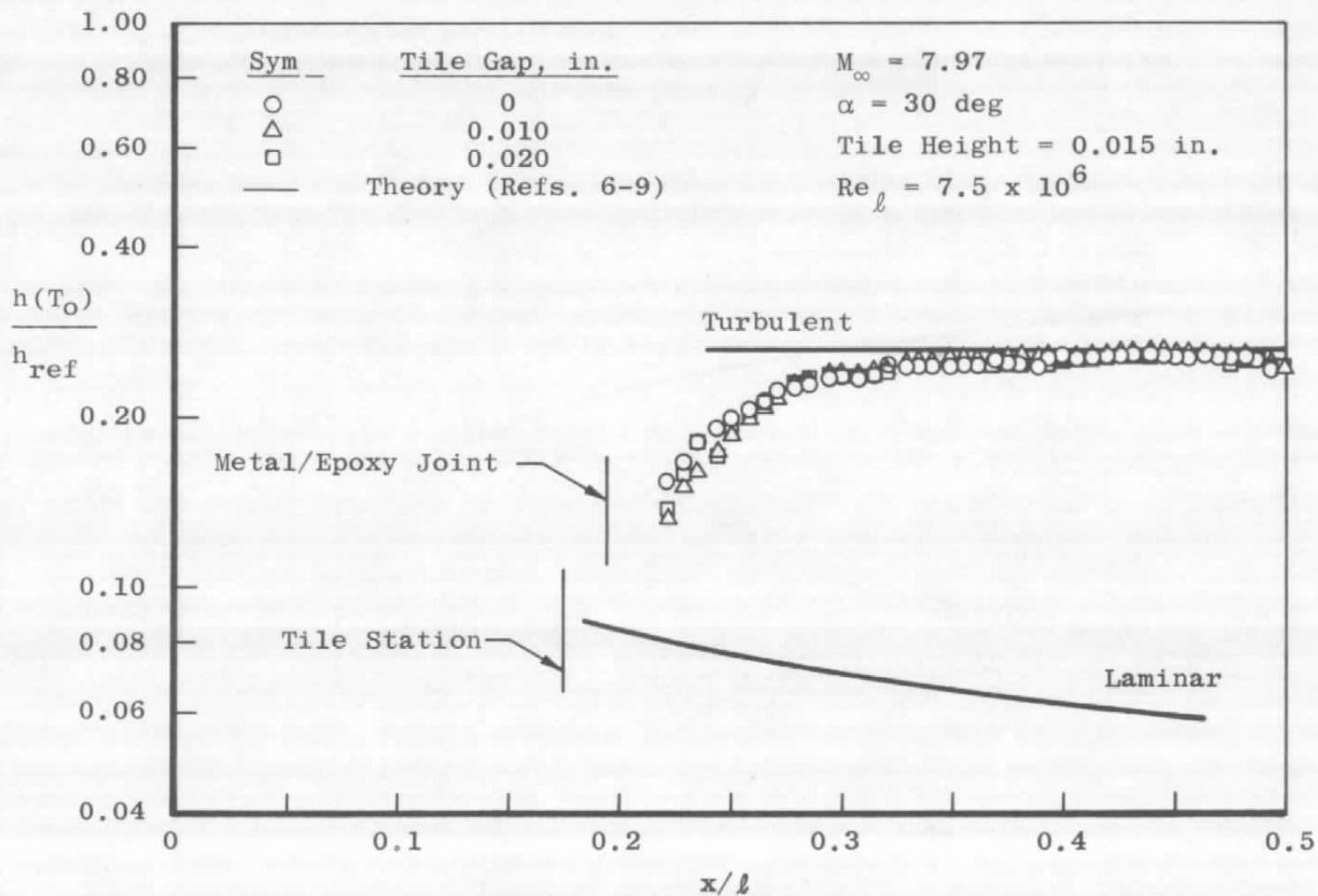
b. Configuration 8, tile x/ℓ = 0.175
Figure 19. Concluded.
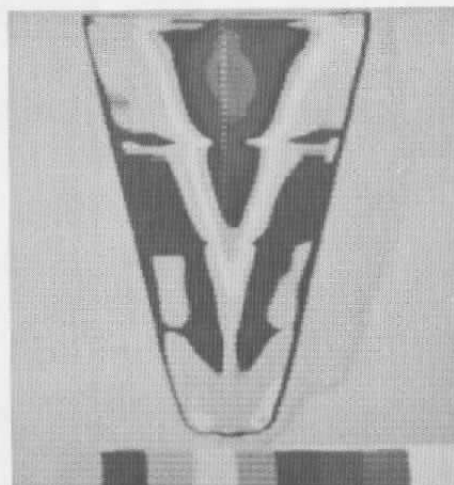
$M_\infty$ = 7.97
Tile Station x/$\ell$ = 0.050
Tile Height = 0.010 in.
$\alpha$ = 30 deg

a.  Tile gap = 0
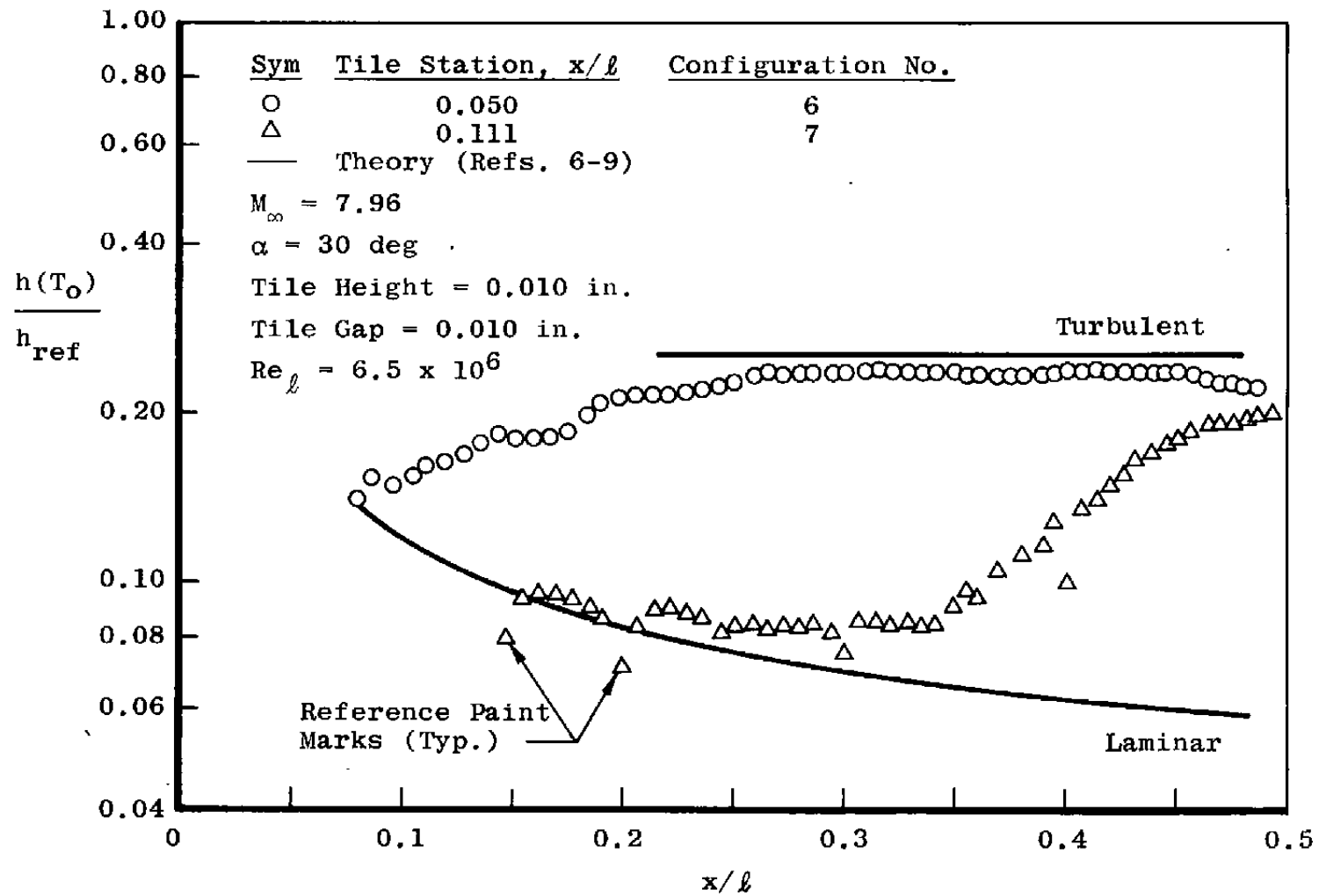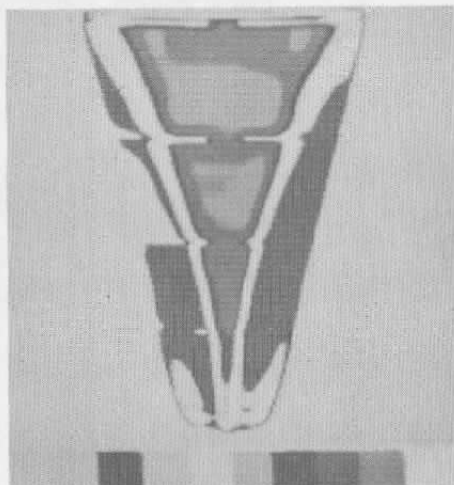
b.  Tile gap = 0.010 in.
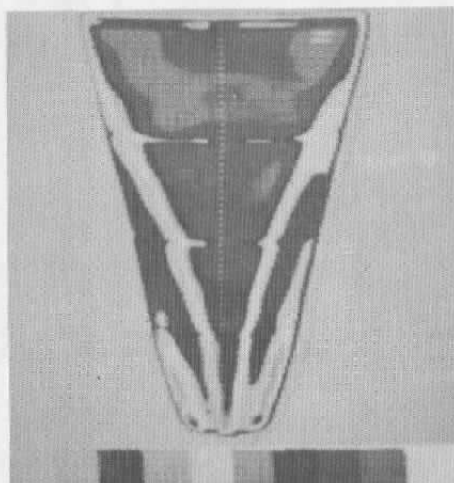
c.  Tile gap = 0.020 in.

Figure 20.  Photographs of windward surface temperature distributions with tile
gap variations at Re$\varrho$ = 7.5 x 10$^6$, $\alpha$ = 30 deg.
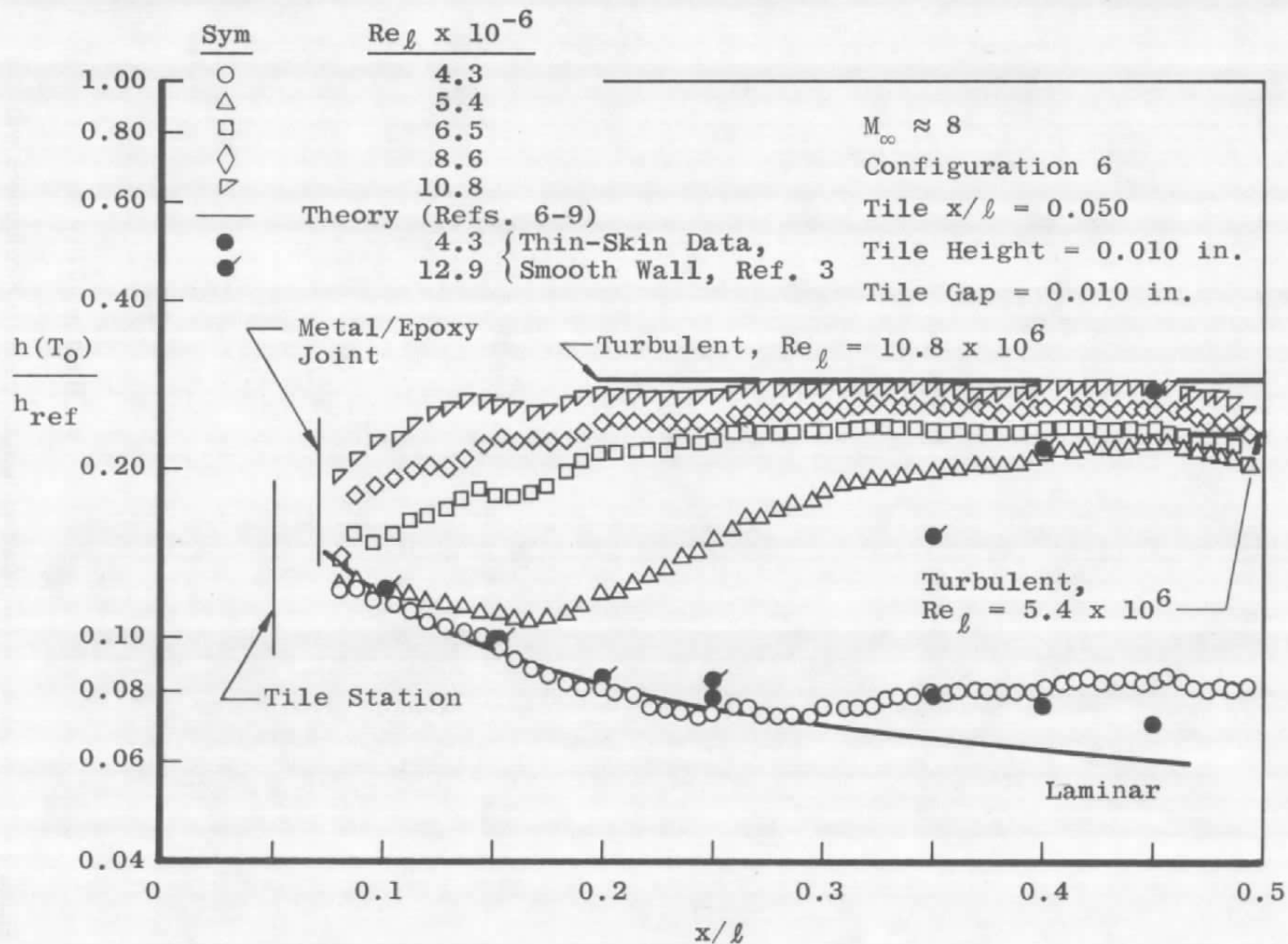
Figure 21. Free-stream Reynolds number variation influence on longitudinal windward centerline
heat-transfer distribution at $a$ = 30 deg.
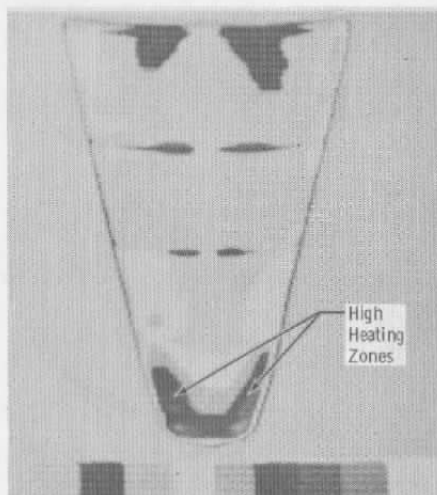
$M_\infty \approx 8$
Configuration 6
Tile $x/\ell$ = 0.050
Tile Height = 0.010 in.
Tile Gap = 0.010 in.

a. $Re_\ell = 4.3 \times 10^6$

b. $Re_\ell = 8.6 \times 10^6$
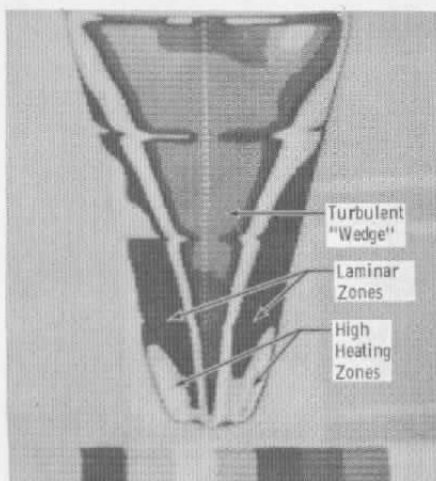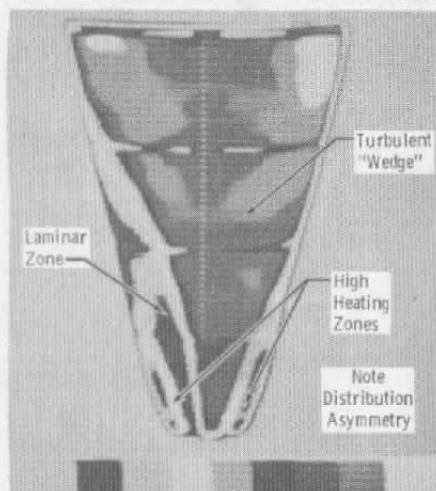
c. $Re_\ell = 10.8 \times 10^6$

Figure 22. Photographs of windward temperature distributions with free-stream Reynolds number variations at $a$ = 30 deg, Configuration 6.
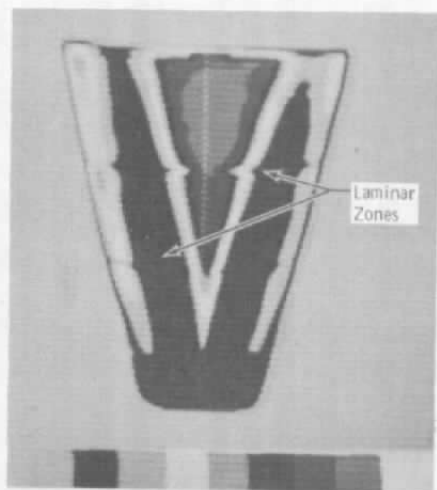
$M_\infty \approx 8$
Configuration 7
Tile $x/\ell$ = 0.111
Tile Height = 0.010 in.
Tile Gap = 0

Laminar Zones

a.  $Re_\ell = 7.5 \times 10^6$

b.  $Re_\ell = 10.8 \times 10^6$
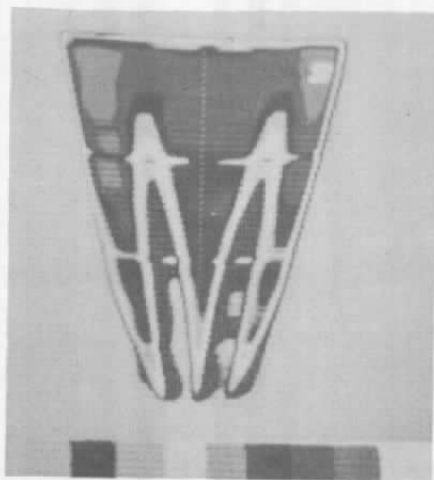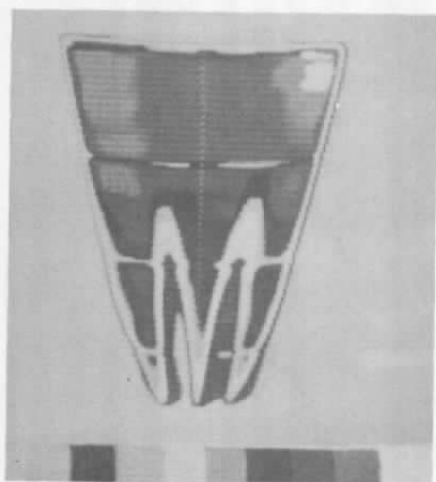
c.  $Re_\ell = 14.0 \times 10^6$

Figure 23.  Photographs of windward surface temperature distributions with free-stream Reynolds number variations at $a$ = 30 deg, Configuration 7.

46
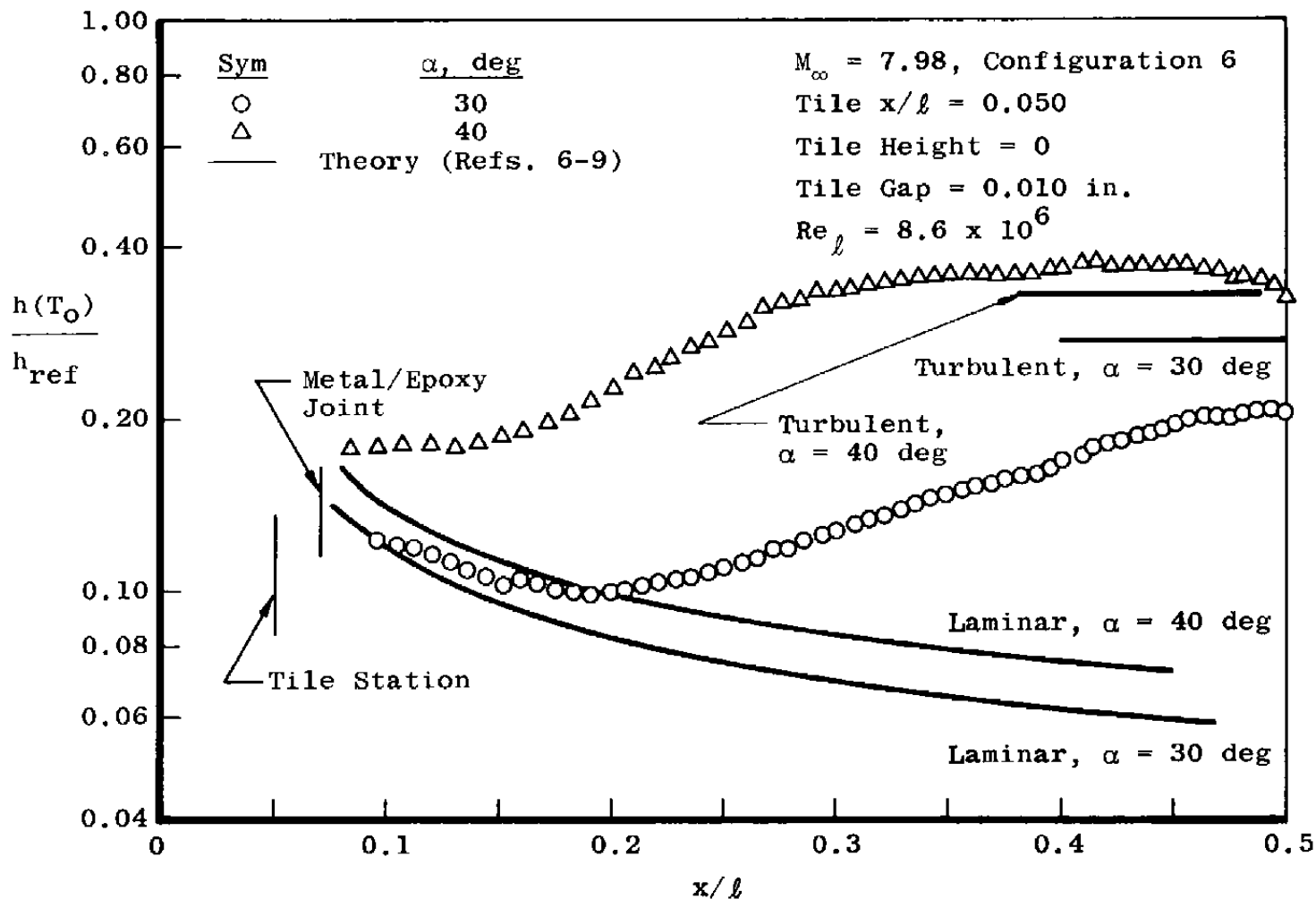
a. Tile height = 0

Figure 24. Angle-of-attack influences on longitudinal windward centerline heat-transfer distributions at $Re_\ell = 8.6 \times 10^6$.
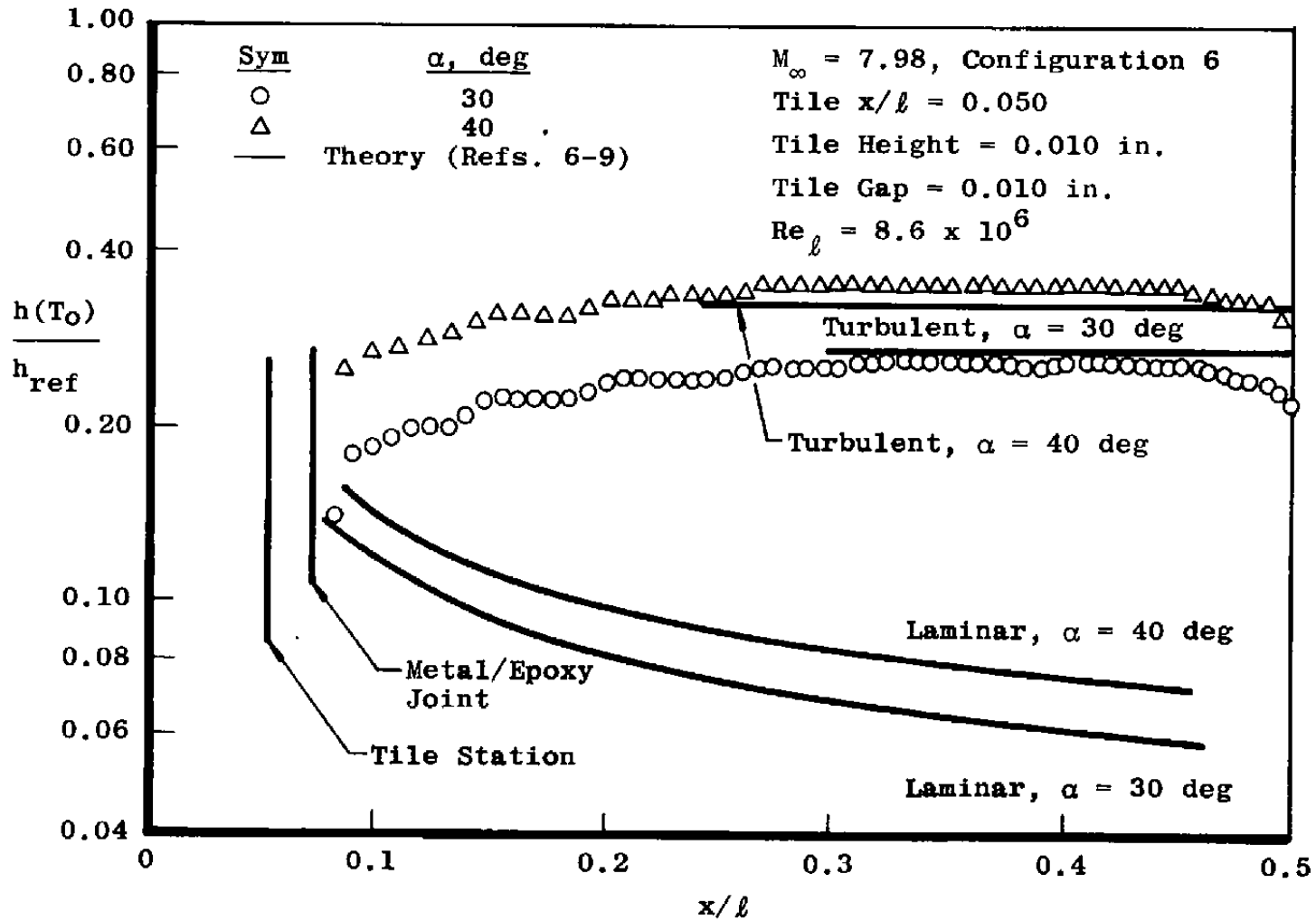
b. Tile height = 0.010 in.
Figure 24. Concluded.
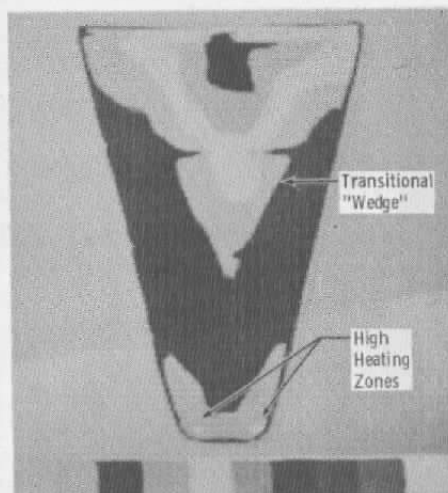
a.  Tile height = 0

Figure 25.  Photographs of windward surface temperature distributions with angle-of-attack variation at $Re_\ell = 8.6 \times 10^6$, Configuration 6.
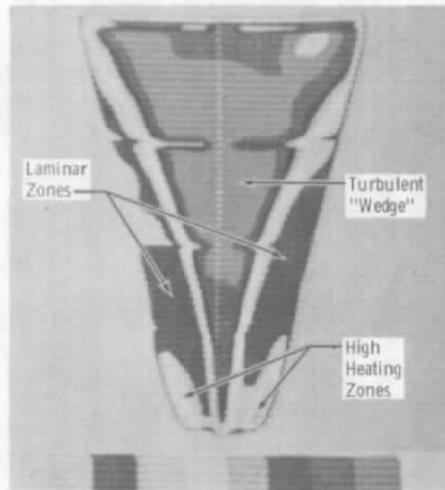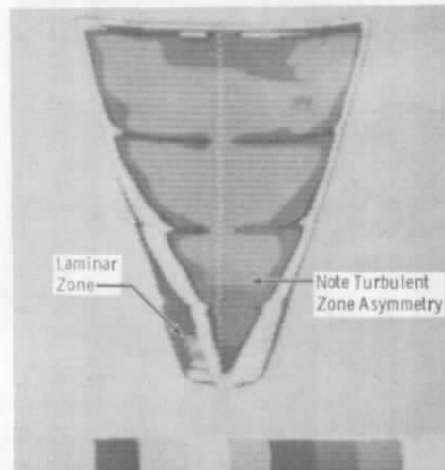
α = 30 deg

α = 40 deg

b.  Tile height = 0.010
Figure 25.  Concluded.
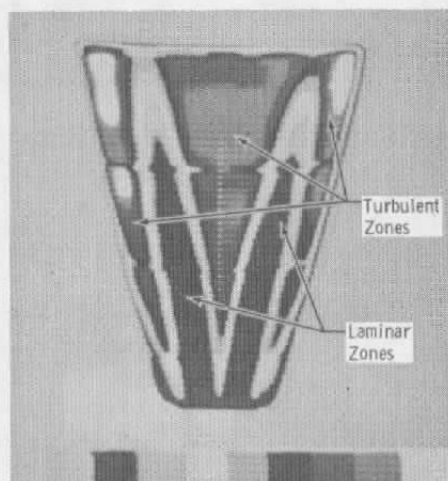
M$_\infty$ = 7.98
Configuration 7
Tile x/$\ell$ = 0.111
Tile Height = 0.010 in.
Tile Gap = 0

a.  $\alpha$ = 30 deg
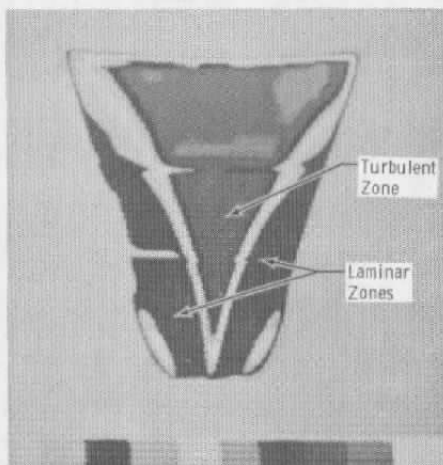
b.  $\alpha$ = 40 deg

Figure 26.  Photographs of windward surface temperature distributions with angle-of-attack variations at Re$_\ell$ = 8.6 x 10$^6$, Configuration 7.
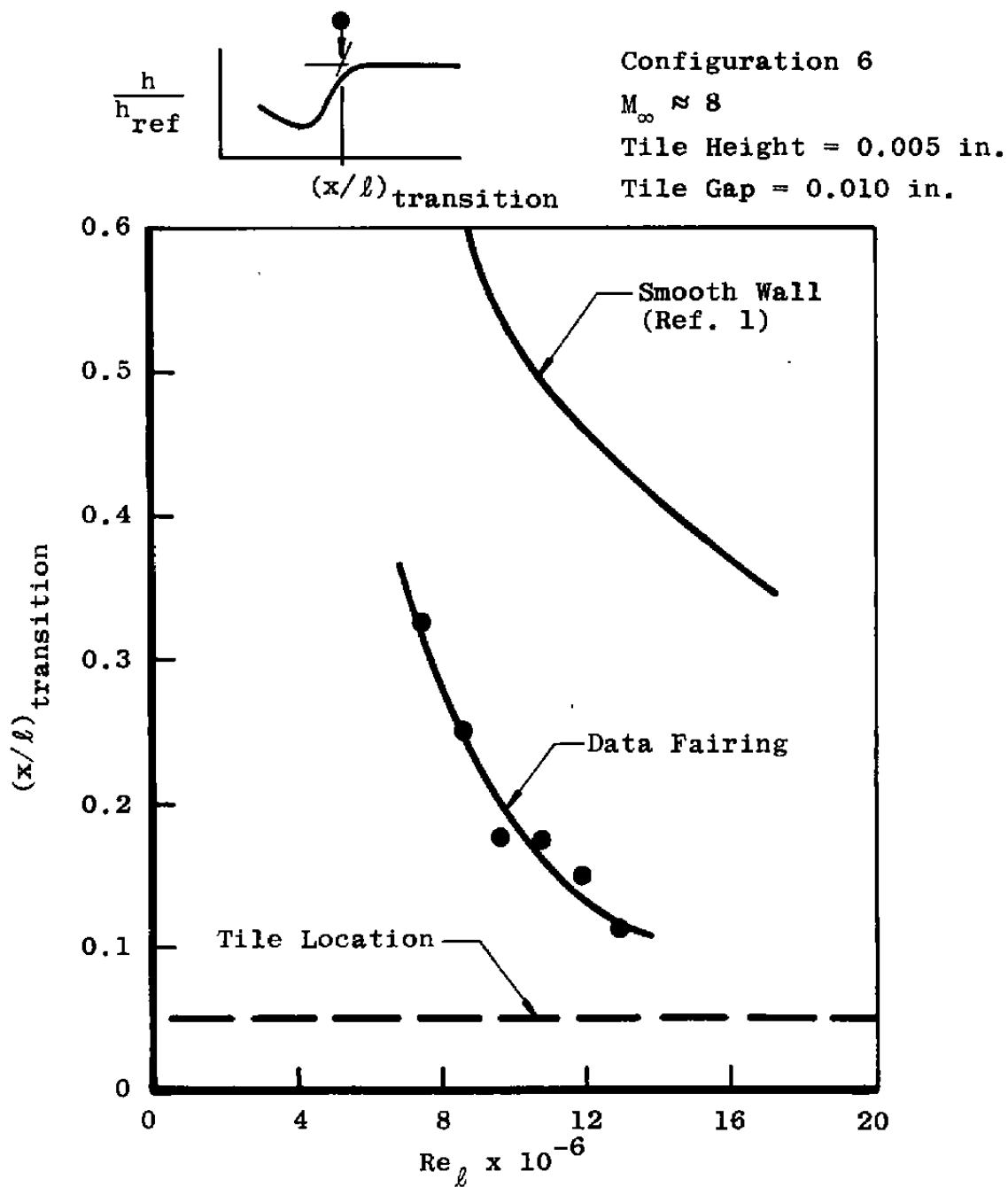
Figure 27. Example of tile tripping effectiveness based on windward centerline heat-transfer distributions at $a$ = 30 deg, Configuration 6.

### Table 1.  Test Summary

| Configuration | Trip x/$\ell$ | Gap | Tile Height | Re$_\ell$ x $10^6$/ft | $\alpha$ |
|---|---|---|---|---|---|
| 6 | 0.050 | 0.010 | 0 | 6.5 | 30 |
| | | | | 6.5 | 40 |
| | | | | 8.6 | 30 |
| | | | | 8.6 | 40 |
| | | | | 12.9 | 30 |
| | | | | 12.9 | 40 |
| 6 | 0.050 | 0.010 | 0.005 | 5.4 | 40 |
| | | | | 5.6 | 30 |
| | | | | 5.6 | 40 |
| | | | | 7.5 | 30 |
| | | | | 7.5 | 40 |
| | | | | 8.6 | 30 |
| | | | | 8.6 | 40 |
| | | | | 9.7 | 30 |
| | | | | 9.7 | 40 |
| | | | | 10.8 | 30 |
| | | | | 10.8 | 40 |
| | | | | 11.9 | 30 |
| | | | | 11.9 | 40 |
| | | | | 12.9 | 30 |
| 6 | 0.050 | 0.010 | 0.010 | 4.3 | 30 |
| | | | | 4.3 | 40 |
| | | | | 5.4 | 30 |
| | | | | 6.5 | 30 |
| | | | | 6.5 | 40 |
| | | | | 7.5 | 30 |
| | | | | 7.5 | 40 |
| | | | | 8.6 | 30 |
| | | | | 8.6 | 40 |
| | | | | 9.7 | 30 |
| | | | | 9.7 | 40 |
| | | | | 10.8 | 30 |
| | | | | 10.8 | 40 |
| | | | | 11.9 | 30 |

Table 1. Continued

| Configuration | Trip $x/\ell$ | Gap | Tile Height | $Re_\ell \times 10^6/ft$ | $\alpha$ |
|---|---|---|---|---|---|
| 6 | 0.050 | 0.010 | 0.015 | 3.2 | 40 |
| | | | | 4.3 | 30 |
| | | | | 4.3 | 40 |
| | | | | 5.4 | 30 |
| | | | | 5.4 | 40 |
| | | | | 6.5 | 30 |
| | | | | 6.5 | 40 |
| | | | | 7.5 | 30 |
| | | | | 7.5 | 40 |
| | | | | 8.6 | 30 |
| | | | | 8.6 | 40 |
| | | | | 9.7 | 30 |
| | | | | 9.7 | 40 |
| | | | | 10.8 | 30 |
| | | | | 10.8 | 40 |
| | | | | 11.9 | 30 |
| 6 | 0.050 | 0 | 0.010 | 7.5 | 30 |
| | | | | 7.5 | 40 |
| | | | | 8.6 | 30 |
| | | | | 8.6 | 40 |
| | | | | 9.7 | 30 |
| | | | | 9.7 | 40 |
| | | | | 10.8 | 30 |
| | | | | 10.8 | 40 |
| | | | | 11.9 | 30 |
| | | | | 11.9 | 40 |
| | | | | 12.9 | 30 |
| | | | | 12.9 | 40 |
| | | | | 14.0 | 30 |
| | | | | 14.0 | 40 |
| | | | | 15.1 | 30 |

Table 1. Continued

| Configuration | Trip $x/\ell$ | Gap | Tile Height | $Re_\ell \times 10^6/ft$ | $\alpha$ |
|---|---|---|---|---|---|
| 6 | 0.050 | 0.020 | 0.010 | 3.2 | 40 |
| | | | | 4.3 | 30 |
| | | | | 4.3 | 40 |
| | | | | 5.4 | 30 |
| | | | | 5.4 | 40 |
| | | | | 6.5 | 30 |
| | | | | 6.5 | 40 |
| | | | | 7.5 | 30 |
| | | | | 7.5 | 40 |
| | | | | 8.6 | 30 |
| | | | | 8.6 | 40 |
| | | | | 9.7 | 30 |
| | | | | 9.7 | 40 |
| | | | | 10.8 | 30 |
| | | | | 11.9 | 30 |
| 7 | 0.111 | 0.010 | -0.020 | 4.3 | 40 |
| | | | | 5.4 | 40 |
| | | | | 6.5 | 30 |
| | | | | 6.5 | 40 |
| | | | | 7.5 | 30 |
| | | | | 7.5 | 40 |
| | | | | 8.6 | 30 |
| | | | | 8.6 | 40 |
| | | | | 9.7 | 30 |
| | | | | 9.7 | 40 |
| | | | | 10.8 | 30 |
| | | | | 10.8 | 40 |
| | | | | 11.9 | 30 |
| 7 | 0.111 | 0.010 | 0 | 4.3 | 30 |
| | | | | 4.3 | 40 |
| | | | | 6.5 | 30 |
| | | | | 6.5 | 40 |
| | | | | 8.6 | 30 |
| | | | | 8.6 | 40 |
| | | | | 12.9 | 30 |
| | | | | 12.9 | 40 |

Table 1. Continued

| Configuration | Trip $x/\ell$ | Gap | Tile Height | $Re\ell \times 10^6/ft$ | $\alpha$ |
|:---:|:---:|:---:|:---:|:---:|:---:|
| 7 | 0.111 | 0.010 | 0.010 | 4.3 | 40 |
| | | | | 5.4 | 30 |
| | | | | 5.4 | 40 |
| | | | | 6.5 | 30 |
| | | | | 6.5 | 40 |
| | | | | 7.5 | 30 |
| | | | | 7.5 | 40 |
| | | | | 8.6 | 30 |
| | | | | 8.6 | 40 |
| | | | | 9.7 | 30 |
| | | | | 9.7 | 40 |
| | | | | 10.8 | 30 |
| | | | | 10.8 | 40 |
| | | | | 11.9 | 30 |
| 7 | 0.111 | 0.010 | 0.015 | 4.3 | 30 |
| | | | | 4.3 | 40 |
| | | | | 5.4 | 30 |
| | | | | 5.4 | 40 |
| | | | | 6.5 | 30 |
| | | | | 6.5 | 40 |
| | | | | 7.5 | 30 |
| | | | | 7.5 | 40 |
| | | | | 8.6 | 30 |
| 7 | 0.111 | 0.010 | 0.020 | 7.5 | 20 |
| | | | | 2.2 | 40 |
| | | | | 3.2 | 30 |
| | | | | 3.2 | 40 |
| | | | | 3.4 | 30 |
| | | | | 4.3 | 30 |
| | | | | 4.3 | 40 |
| | | | | 5.4 | 30 |
| | | | | 5.4 | 40 |
| | | | | 6.5 | 30 |
| | | | | 6.5 | 40 |
| | | | | 7.5 | 30 |
| | | | | 8.6 | 30 |
| | | | | 8.6 | 40 |
| | | | | 12.9 | 30 |

## Table 1. Continued

| Configuration | Trip $x/\ell$ | Gap | Tile Height | $Re_\ell \times 10^6/ft$ | $\alpha$ |
|:---:|:---:|:---:|:---:|:---:|:---:|
| 7 | 0.111 | 0 | 0.010 | 5.4 | 40 |
| | | | | 6.5 | 40 |
| | | | | 7.5 | 30 |
| | | | | 7.5 | 40 |
| | | | | 8.6 | 30 |
| | | | | 8.6 | 40 |
| | | | | 9.7 | 30 |
| | | | | 9.7 | 40 |
| | | | | 10.8 | 30 |
| | | | | 10.8 | 40 |
| | | | | 11.9 | 30 |
| | | | | 12.9 | 30 |
| ↓ | ↓ | ↓ | ↓ | 14.0 | 30 |
| 7 | 0.111 | 0.020 | 0.010 | 4.3 | 40 |
| | | | | 5.4 | 30 |
| | | | | 5.4 | 40 |
| | | | | 6.5 | 30 |
| | | | | 6.5 | 40 |
| | | | | 7.5 | 30 |
| | | | | 7.5 | 40 |
| | | | | 8.6 | 30 |
| | | | | 8.6 | 40 |
| | | | | 9.7 | 30 |
| ↓ | ↓ | ↓ | ↓ | 10.8 | 30 |
| 7 | 0.111 | 0.010 | 0.010 | 7.5 | 30 |
| | | | | 7.5 | 40 |
| | | | | 8.6 | 30 |
| | | | | 8.6 | 40 |
| | | | | 10.8 | 30 |
| ↓ | ↓ | ↓ | ↓ | 10.8 | 40 |

Table 1. Continued

| Configuration | Trip x/$\ell$ | Gap | Tile Height | Re$_\ell$ x 10$^6$/ft | $\alpha$ |
|---|---|---|---|---|---|
| 8 | 0.175 | 0.010 | -0.020 | 5.4 | 40 |
| | | | | 6.5 | 40 |
| | | | | 7.5 | 40 |
| | | | | 8.6 | 30 |
| | | | | 8.6 | 40 |
| | | | | 9.7 | 30 |
| | | | | 9.7 | 40 |
| | | | | 10.8 | 30 |
| | | | | 10.8 | 40 |
| | | | | 11.9 | 30 |
| | | | | 11.9 | 40 |
| | | | | 12.9 | 30 |
| | | | | 12.9 | 40 |
| | | | | 14.0 | 30 |
| | | | | 15.1 | 30 |
| 8 | 0.175 | 0.010 | 0.010 | 4.3 | 40 |
| | | | | 5.4 | 30 |
| | | | | 5.4 | 40 |
| | | | | 6.5 | 30 |
| | | | | 6.5 | 40 |
| | | | | 7.5 | 30 |
| | | | | 7.5 | 40 |
| | | | | 8.6 | 30 |
| | | | | 8.6 | 40 |
| | | | | 9.7 | 30 |
| | | | | 9.7 | 40 |
| | | | | 10.8 | 30 |
| | | | | 10.8 | 40 |
| | | | | 11.9 | 30 |
| | | | | 11.9 | 40 |
| | | | | 12.9 | 30 |

## Table 1. Continued

| Configuration | Trip x/$\ell$ | Gap | Tile Height | Re$_\ell$ x $10^6$/ft | $\alpha$ |
|:---:|:---:|:---:|:---:|:---:|:---:|
| 8 | 0.175 | 0.010 | 0.015 | 3.2 | 40 |
| | | | | 4.3 | 30 |
| | | | | 4.3 | 40 |
| | | | | 5.4 | 30 |
| | | | | 5.4 | 40 |
| | | | | 6.5 | 30 |
| | | | | 6.5 | 40 |
| | | | | 7.5 | 30 |
| | | | | 7.5 | 40 |
| | | | | 8.6 | 30 |
| | | | | 8.6 | 40 |
| | | | | 9.7 | 30 |
| | | | | 9.7 | 40 |
| | | | | 10.8 | 30 |
| | | | | 10.8 | 40 |
| | | | | 11.9 | 30 |
| | | | | 11.9 | 40 |
| | | | | 12.9 | 30 |
| 8 | 0.175 | 0.010 | 0.025 | 2.2 | 40 |
| | | | | 3.2 | 30 |
| | | | | 3.2 | 40 |
| | | | | 4.3 | 30 |
| | | | | 4.3 | 40 |
| | | | | 5.4 | 30 |
| | | | | 5.4 | 40 |
| | | | | 6.5 | 30 |
| | | | | 6.5 | 40 |
| | | | | 7.5 | 30 |
| | | | | 7.5 | 40 |
| | | | | 8.6 | 30 |
| | | | | 8.6 | 40 |
| | | | | 9.7 | 30 |
| | | | | 9.7 | 40 |
| | | | | 10.8 | 30 |
| | | | | 11.9 | 30 |

**Table 1. Concluded**

| Configuration | Trip $x/\ell$ | Gap | Tile Height | $Re_\ell$ x $10^6$/ft | $\alpha$ |
|:---:|:---:|:---:|:---:|:---:|:---:|
| 8 | 0.175 | 0 | 0.015 | 3.2 | 40 |
| | | | | 4.3 | 30 |
| | | | | 4.3 | 40 |
| | | | | 5.4 | 30 |
| | | | | 5.4 | 40 |
| | | | | 6.5 | 30 |
| | | | | 6.5 | 40 |
| | | | | 7.5 | 30 |
| | | | | 7.5 | 40 |
| | | | | 8.6 | 30 |
| | | | | 8.6 | 40 |
| | | | | 9.7 | 30 |
| | | | | 9.7 | 40 |
| | | | | 10.8 | 30 |
| | | | | 10.8 | 40 |
| | | | | 11.9 | 30 |
| | | | | 11.9 | 40 |
| 8 | 0.175 | 0.020 | 0.015 | 2.2 | 40 |
| | | | | 3.2 | 40 |
| | | | | 4.3 | 30 |
| | | | | 4.3 | 40 |
| | | | | 5.4 | 30 |
| | | | | 5.4 | 40 |
| | | | | 6.5 | 30 |
| | | | | 6.5 | 40 |
| | | | | 7.5 | 30 |
| | | | | 7.5 | 40 |
| | | | | 8.6 | 30 |
| | | | | 8.6 | 40 |
| | | | | 9.7 | 30 |
| | | | | 9.7 | 40 |
| | | | | 10.8 | 30 |
| | | | | 10.8 | 40 |
| | | | | 11.9 | 30 |

## NOMENCLATURE

| | |
|---|---|
| $C_p$ | Model material specific heat, Btu/lbm-°R |
| $h(T_o)$ | Heat-transfer coefficient based on tunnel stilling chamber temperature, Btu/ft$^2$-sec-°R |
| k | Model material conductivity, Btu/ft-sec-°R |
| $\ell$ | Scaled orbiter length, 51.7 in. |
| $M_\infty$ | Free-stream Mach number |
| $P_o$ | Stilling chamber pressure, psia |
| $Re_\ell$ | Free-stream Reynolds number based on scaled orbiter length |
| T | Temperature, °R |
| t | Time, sec |
| x | Axial distance from model nose, in. |
| $(x/\ell)_{transition}$ | Axial distance to the end of transition (see Fig. 27) |
| y | Lateral distance |
| $y_{max}$ | Half-span length at each axial station (see Fig. 6) |
| $\alpha$ | Angle of attack, deg |
| $\beta$ | Semi-infinite solid heat-transfer parameter, $\beta = h(T_o)\sqrt{t}/\sqrt{\rho C_p k}$ |
| $\delta$ | Boundary-layer thickness, in. |
| $\rho$ | Model material density, lbm/ft$^3$ |

## SUBSCRIPTS

| | |
|---|---|
| i | Initial conditions |
| o | Stilling chamber conditions |
| ref | Heat-transfer based on Fay-Riddell theory and 1-ft-radius sphere scaled to model scale (i.e. 0.040 ft) |
| w | Wall conditions |
| $\infty$ | Free-stream conditions |